ORIGINAL PAPER

Crack Coalescence Mechanism and Crack Type Determination Model Based on the Analysis of Specimen Apparent Strain Field Data

Tao Dong[1,2] · Ju Wang[2] · Weiming Gong[1] 🄐 · Fei Wang[3] · Hongguang Lin[4] · Wengbo Zhu[1]

Abstract

Clarifying the crack coalescence mechanism and defining crack types within flawed rock formations offer significant advantages for understanding the failure process of geomaterials in practical geotechnical engineering. This article presents experimental results of red sandstone specimens subjected to uniaxial compression, featuring pre-existing flaws of varying width and inclination. Then, the divided displacement trend line (DDTL) model and crack influencing factors (CIF) model were established to quantitatively investigate the coalescence mechanisms and types of cracks. In addition, the above innovative model was corroborated from a microscopic perspective using the AF-RA method. Test results reveal that most cracks in the initiation stage undergo alternating influences of tensile and shear forces, ultimately coalescing due to a dominant factor. The augmentation in flaw width significantly impacts the displacement at the flaw tip, leading to an increased proportion of shear cracks within the specimen. The CIF model quantitatively analyzes the dominant factor at different sections along a crack and determines whether the crack behavior is influenced by tensile stress (CIF > 0) or shear stress (CIF < 0). The final CIF peak value of tensile cracks generally surpasses 6, while that of shear cracks typically hovers around 0. For mixed cracks primarily dominated by tension, the final CIF peak value generally exceeds 4, while for those primarily dominated by shear, the value is lower than 2. Based on the comprehensive analysis of DDTL model and CIF model, the study identifies five distinct types of cracks: T type, S type, TS type, ST-space type, and ST-time type. These classification models provide a foundation for subsequent investigations on crack propagation mechanisms and are of significant reference value for understanding the failure mechanism of geotechnical engineering under loading conditions.

Highlights

- A quantitative calculation model for determining the crack type was established, and the dominant factors in the crack coalescence process were quantitatively studied.
- The crack influencing factors model can be used to illustrate the factors that dominate crack coalescence. The crack initiation is mostly the result of alternating tensile and shear effects, while the final crack coalescence is generally caused by one of the tensile or shear factors.
- The cracks are classified into: tensile type, shear type, tensile-shear type, shear-tensile space type and shear-tensile time type by the differences of the dominant factors in the initiation, propagation, and coalescence stages of cracks.
- The divided displacement trend line model visualizes the crack coalescence process and validates the rationality of crack influencing factors.

✉ Weiming Gong
  D101004924@163.com

✉ Fei Wang
  wangfei0826@163.com

1   School of Civil Engineering, Key Laboratory of Concrete and Prestressed Concrete Structures of Ministry of Education, Southeast University, Nanjing 211189, China

2   School of Resources and Safety Engineering, Central South University, Changsha 410083, China

3   School of Water Conservancy and Transportation, Zhengzhou University, Zhengzhou 450001, China

4   China Railway Design Corporation, Tianjin 300308, China

1 Introduction

The damage and failure of rock masses in geotechnical engineering predominantly occur due to crack initiation, propagation, and coalescence. Proficient comprehension of crack types and quantities present within engineering rock masses aids in evaluating the extent of damage to engineering components (Dong et al. 2022; Zhou et al. 2019). Additionally, investigating the formation processes and coalescence mechanisms of various crack types is crucial for assessing the safety of rock engineering projects (Nikolic and Ibrahimbegovic 2015). Early scholars categorized cracks based on the order of their appearance, designating them as either primary or secondary cracks (Ingraffea and Heuze 1980). As researchers delved into the mechanisms of crack propagation, they renamed these types as either tensile or shear cracks (Jiefan et al. 1990). Determining the crack initiation mode largely relies on observations of the crack surface due to limitations in measurement techniques. A clean crack surface or one exhibiting a plugging structure leads to the classification of a tensile crack. Conversely, when the surface appears rough or is covered with powder, the crack type is designated as a shear crack (Bobet and Einstein 1998).

However, identifying rock crack types solely based on the geometric features, surface characteristics, propagation direction, and crack displacement is subjective and may result in potential misjudgments of crack identification. For instance, secondary cracks typically propagate as shear cracks on the same plane, but their geometric shape occasionally leads to misclassification as either tensile or shear cracks propagating out of the plane (Bobet and Einstein 1998). Furthermore, as specimens become more complex in structure and subjected to more intricate loading conditions, the resulting types of cracks, such as compression-shear cracks (Zhou et al. 2014a), out-of-plane shear cracks (Zhou et al. 2015), quasi-coplanar secondary cracks (Ha et al. 2015), and oblique secondary cracks (Cao et al. 2015; Haeri et al. 2014), also become more intricate, making it difficult to determine the exact mechanism of crack propagation (Cao et al. 2015, 2020; Lin et al. 2021; Zhou et al. 2014b). Cracks that develop in brittle rocks due to flaws are influenced by multiple types of stresses, including tensile, compressive, and shear stresses (Zhao et al. 2014). This indicates that cracks exhibit diverse properties. The term "mixed cracks" is often used to describe these situations, but a standardized method for determining the dominant stress within mixed cracks has not yet been established (Zhou et al. 2020; Wong and Einstein 2009). This ambiguity reverberates into the exploration of crack coalescence mechanisms, potentially hindering future research.

Advancements in observation techniques have allowed for more detailed crack analysis, revealing that seemingly simple crack formations actually involve complex deformation processes (Wu and Wong 2012; Zhang and Wong 2011). However, the conventional method of observing cracks in rocks has various limitations, such as a restricted strain measurement range, limited observation coverage area, cumbersome operation, sensitivity to temperature, and data loss after crack initiation. To overcome these limitations, researchers have proposed the use of digital image correlation (DIC) as a non-contact optical measurement technique (Chu et al. 1985; Peters and Ranson 1982; Zhang et al. 2022; Si et al. 2024). Zhou et al. (2022a) monitored the real-time cracking process of defective rocks and analyzed the mechanical properties of rocks, cracking behavior, fatigue damage mechanisms, and deformation field evolution characteristics. Additionally, Zhou et al. (2022b) systematically investigated the influence of geometric parameters and flaw angles on the cracking process, demonstrating that wing cracks are primarily dominated by tensile strain, while the initiation mechanisms of anti-wing cracks and secondary cracks are primarily mixed tensile-shear. Sharafisafa et al. (2018) investigated the coalescence behavior of double-defect specimens using displacement vector obtained by DIC, revealing that the reason for the occurrence of tensile or shear cracks is the local tensile or compressive strain concentration at the defect tip or bridge region. Miao et al. (2022) validated the effectiveness and robustness of displacement-based field fitting methods and J-integral methods employing a composite image of Type I cracks acquired through DIC. However, Shams et al. (2023a) revealed experimentally that cracks conventionally considered as tensile fracture at the macroscopic scale are actually consist of three main cracking mechanisms at the microscopic scale, including tensile, shear, and compression sources. Therefore, relying solely on the analysis of the surface strain field of the specimen cannot fully reveal the fracture mechanism of the crack.

With the widespread application of acoustic emission (AE) equipment, it has become a valuable tool in monitoring the evolution of internal cracks within test specimens. Zafar et al. (2022a) utilized this equipment to assess the temporal and spatial evolution of crack mechanisms, revealing a high evolution of tensile cracks at different stages of creep and relaxation. Ohno and Ohtsu (2010) made a significant breakthrough in concrete crack classification by leveraging AE data, employing a parameter-based method, and harnessing simplified Green's functions. Zhang and Deng (2020) introduced an innovative approach for ascertaining the optimal transition line of crack classification during AE parameter analysis. Combining DIC with AE testing apparatus provides an effective solution to overcome the limitations of DIC in monitoring the internal coalescence

of cracks within specimens. Based on the combination of DIC equipment with the AE equipment, Zafar et al. (2022b) tracked the mechanism of stress-induced crack coalescence, discovering a quantitative correlation between visual and acoustic observations. Qian et al. (2022) found that the moisture content affects the extent of crack growth, while joint inclination influences the crack type. Shams et al. (2023b) conducted observations on microcracks under both indirect and direct tensile loading conditions. Through tensor inversion analysis, they found that the so-called tensile macro-fracture mainly consists of shear microcracks and tensile microcracks. In addition, the rock fracture evolution mechanisms determined by the AF–RA method are consistent with the results obtained through the moment tensor inversion method (Cheng et al. 2023). In addition to employing more advanced monitoring equipment, researchers often use the method of prefabricating fissures in specimens to induce noticeable cracking. For example, Shi et al. (2022) analyzed the fracture mode and damage evolution process of jointed sandstone specimens in multilevel cyclic tests (MCT) and fatigue-creep tests (FCT), observing the influence of creep load on crack type. Wang et al. (2022a) examined the fatigue damage and fracture evolution characteristics of red sandstone, revealing different crack extension behaviors of specimens containing joints with different inclination angles. Specifically, joints with inclination angles of 0° and 30° predominantly exhibited tensile fracture, while those with angles of 60° and 90° exhibited predominantly shear fracture (Wang et al. 2022b).

Until now, the quantitative characterization of various crack types remains inadequately researched. A particularly challenging issue arises with mixed type cracks that exhibit both tensile and shear characteristics, making it difficult to classify them, track their evolution, and predict specimen failure modes. To address these issues, this study conducted a quantitative determination of crack types for different cracks generated in red sandstone specimens containing flaws. Through the amalgamation of macroscopic and microscopic mechanics perspectives, the investigation into the coalescence mechanism of different rock crack types stands as a crucial cornerstone for unraveling the intricate rock fracture mechanism. First, utilizing the AE data, the crack coalescence inside the specimen was meticulously counted from a microscopic perspective. Subsequently, a divided displacement trend line (DDTL) model was proposed, facilitating the visualization and analysis of crack initiation and propagation. Finally, an innovative crack influencing factors (CIF) calculation model was established based on the displacement patterns around the crack, aiming to quantify the disparities in the initiation, propagation, and coalescence among various crack types. In this way, crack types (i.e. tensile cracks, shear cracks, or mixed tensile-shear cracks) can be accurately determined by combining qualitative and

Table 1 Experimental mechanical properties of tested red sandstone

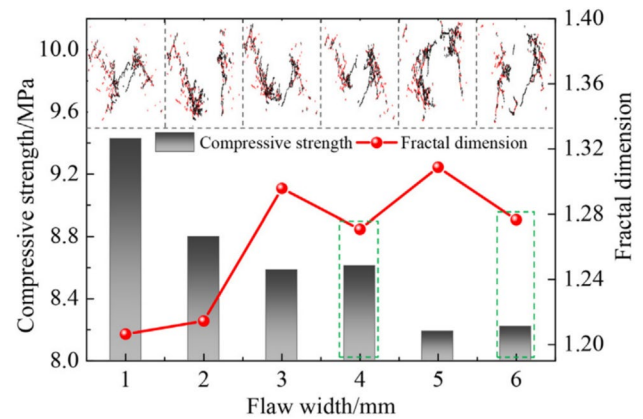| Unit weight γ (kN/m³)	Uniaxial compressive strength σ_e (MPa)	Brazilian tensile strength σ_t (MPa)	Young's modulus E (GPa)	Poisson's ratio v
24.64 ± 0.8	75.28 ± 2.80	4.68 ± 0.20	17.24 ± 2.26	0.18 ± 0.01

Fig. 1 The relationship between the compressive strength, fractal dimension, and the flaw width (Liu et al. 2015)

quantitative methods. This research significantly contributes to the prognostication of crack coalescence behavior in various structures, such as rocky slopes, tunnels, foundations, particularly in geological conditions that are prone to flaws. The study provides a valuable approach for future investigations, guaranteeing accurate characterization and coalescence mechanism analysis of diverse crack types.

2 Experimental Methodology

2.1 Specimens Selection

The red sandstone utilized in this experiment was obtained from Linfen City, Shandong Province, China. Uniaxial compression and Brazilian disk tests were performed on the red sandstone specimens, and the basic mechanical parameters obtained are presented in Table 1. To minimize the influence of end friction on the test results as much as possible, the aspect ratio of the specimens was selected to be 2.0, in compliance with the recommended method of the International Society for Rock Mechanics and Rock Engineering (ISRM) testing procedures (Wong and Einstein. 2009). The red sandstone was cut using a precision cutting instrument, and the dimensions (height × width × thickness) of the tested specimens were standardized at $80 \times 40 \times 40$ mm. Previous research on crack propagation patterns, compressive strength, and fractal dimensions at different defect widths is

depicted in Fig. 1 (Liu et al. 2015). From the fractal dimension analysis, it can be observed that 3 mm is the critical width at which the flaw width starts influencing the fractal dimension. As the flaw width increases, it can no longer be considered as a joint defect, but rather a hole defect. Therefore, the flaw widths utilized in this experiment were set to 1.5 mm and 4.0 mm. Various flaws, differing in widths and angles, were intentionally introduced at the center of the specimens. The inclination angles α of the flaws were set to 0°, 45°, and 90°, with a flaw length of 15 mm. Figure 2a represents the geometric diagram of the specimen size utilized in this experiment. Due to the monitoring instrument could not directly recognize the microscopic changes on the surface of the red sandstone, speckle patterns were created on the surface of the specimens to facilitate the identification of the monitoring instrument (Baqersad et al. 2017; Wu and Fan. 2020). The speckle patterns were generated employing a spray paint method, creating a distinct black and white contrast on the surface of the specimens, as illustrated in Fig. 2b. The specific steps were as follows: a smooth and flat surface of the specimen was selected as the data collection surface for the global strain field. Subsequently, after the paint had fully dried, sporadic black spots were sprayed onto the white paint using matte black paint. This process ensured

an even distribution of black spots across the white paint, establishing the desired speckle pattern for strain analysis.

The set of testing specimens consisted of six distinct types of flaws, each comprising three specimens, in addition to two intact specimens of identical size. Each specimen was assigned a unique identifier based on its specific characteristics. The specimens marked with "S" depict those with a flaw width of 1.5 mm, while those labeled with "SC" represent those with a flaw width of 4.0 mm. The specimen identification number contains information about the flaw inclination angle and the specimen number. For instance, the SC-45-2 specimen signifies the second specimen with a flaw width of 4.0 mm and a flaw inclination angle of 45°. All the specimen identification numbers utilized in the experiment are detailed in Table 2.

2.2 Loading Equipment and Sensor Settings

The testing equipment primarily included a testing loading system, an AE system, and a DIC system, as illustrated in Fig. 3. Uniaxial compression tests were conducted on sandstone specimens with pre-existing flaws using a rock mechanics servo control system and a DCS-200 loading system. The load was regulated through feedback data from the pressure system and a desktop computer within the servo control system. The loading rate for all specimens was set at 200 N/s.

The AE system employed a PCI-II AE device manufactured by Physical Acoustics Corporation of the United States. Two Nano30 AE probes with a frequency range of 125–750 kHz were used to capture the AE signals emitted from inside the specimens. These probes were, respectively, fixed at 20 mm away from the upper and lower ends of rock specimens by the magnetic clamping device, and Vaseline was used as the coupling agent to eliminate the effect of end face friction. To minimize electronic or environmental noise, the AE signal detection threshold and pre-amplification gain were set to 45 dB and 40dB, respectively. Moreover, the sampling frequency of the AE monitoring system was set
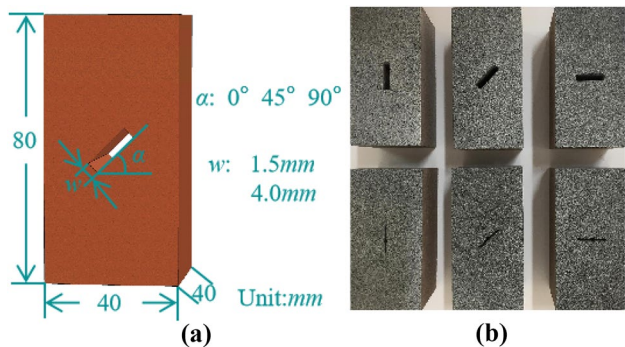

Fig. 2 Images of specimens: **a** geometric diagram of the specimen; **b** specimen physical diagram

Table 2 Tested specimens under uniaxial compression

Specimen ID	Flaw width	α	Specimen ID	Flaw width	α
S-0-1	1.5 mm	0°	SC-0–1	4.0 mm	0°
S-0-2			SC-0-2		
S-0-3			SC-0-3		
S-45-1		45°	SC-45-1		45°
S-45-2			SC-45-2		
S-45-3			SC-45-3		
S-90-1		90°	SC-90-1		90°
S-90-2			SC-90-2		
S-90-3			SC-90-3		
Intact specimens-1	–	–	Intact specimens-2	–	–

Fig. 3 Layout of the loading equipment and sensor settings

Nano30 AE probe

PCI-II AE device
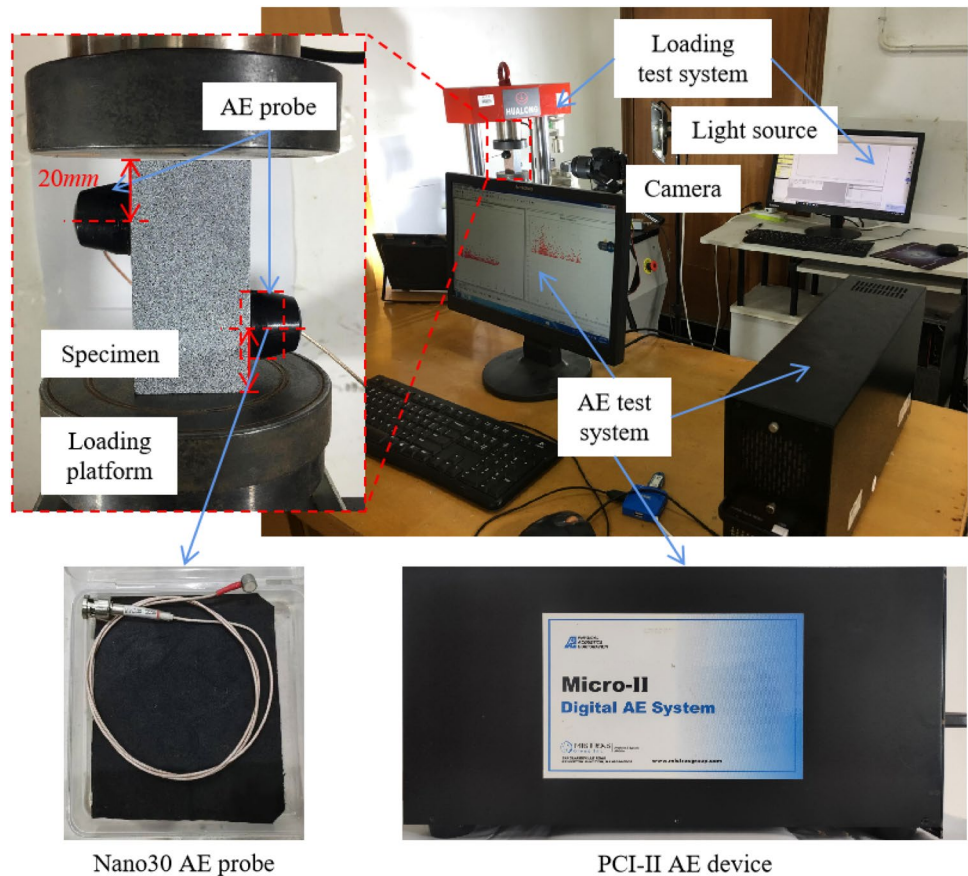
at 10MHz. The efficacy of the coupling between AE probes and the rock surface was verified through a lead breaking test conducted prior to loading.

The DIC method is a non-contact optical approach used for accurately determining strain and displacement fields. This method primarily involves an industrial-grade camera, two LED light sources, and Vic-2D processing software. To ensure that the camera can focus to capture the entire surface of the specimen clearly and completely, the camera was placed at a distance of 0.5 m from the specimen surface. The camera's resolution was set to 3384×2740 pixels, and the rapid acquisition frame rate was set to 60 frames per second. The LED light sources were strategically placed on both sides of the loading device to illuminate the specimen surface adequately. The Vic-2D processing software can measure in-plane displacements and strains over 2000% deformation with a measurement resolution as low as 10 microstrains. This software utilizes image matching techniques and alignment algorithms (Gao et al. 2021) to process a series of continuously varying images of spots obtained during the experiment. In the processing setup of Vic-2D software, three important concepts are involved: the region of interest (ROI), subsets for tracking the displacement change between image analysis regions and steps for controlling the distance between pixel points in the analysis

calculation (Aliabadian et al. 2019; Sharafisafa et al. 2018). To ensure the quality of the results, the surface with the defective area removed was used as the ROI. The parameter settings for subsets and steps are derived from the preprocessing recommendations of the Vic-2D software (Dong et al. 2023), and they were set to 21 and 5, respectively.

3 Method Description for Determining Crack Type

3.1 Description of the Method Based on AE

As widely acknowledged, the parameters of the AE signal are closely related to the type and extension state of internal cracks in rocks. Therefore, through the observation of variations in AE signal parameters generated by cracks under distinct mechanical mechanisms, the crack types of the material can be distinguished. The identification of crack types can be achieved through the definition of AE parameters (Du et al. 2020), with AF value and RA value being the most commonly used AE-derived parameters for material fracture mode analysis, as shown in Eq. (1) and Eq. (2), respectively:

$$AF = AEC/Du, \tag{1}$$

$$RA = RT/Am, \qquad (2)$$

where AF denotes the ratio of AE count to duration, AEC denotes the count of AE signals, Du denotes duration time, RA denotes the ratio of rise time to amplitude, RT denotes rise time, Am denotes amplitude. The physical meaning of the above AE parameters is illustrated in Fig. 4a.

Currently, crack classification methods based on AF and RA values have been widely applied to analyze the fracture mechanism of rock materials (Liu et al. 2020; Wang et al. 2021). Numerous studies have suggested that AE signals generated by shear cracks exhibit high rise time and low frequency, while those from tensile cracks exhibit the opposite characteristics (Niu et al. 2020; Wang et al. 2021, 2022a; Long et al. 2023). In general, shear cracks propagate mainly in the form of shear waves, resulting in high RA values, while tensile cracks propagate primarily in the form of longitudinal waves, resulting in low RA values. In short, tensile cracks have higher AF values, while shear cracks have higher RA values (Ohno and Ohtsu. 2010). The crack classification method based on AF and RA values is shown in Fig. 4b. The proportion of tensile cracks is represented by the percentage of AE events above the dividing line, the shear crack proportion by the percentage of AE events below the dividing line, and the mixed crack proportion by the percentage of AE events in the transition zone along the dividing line (Shi et al. 2023). Currently, there is no unified standard for the boundary line. Studies have shown that the ratio of AF to RA for the crack boundary of brittle materials ranged from 100:1 to 500:1 (Zhang and Deng. 2020). Consequently, this study adopts a slope of 100 for the boundary line.

3.2 Description of Divided Displacement Trend Line (DDTL) Model

The utilization of displacement vectors significantly enhances the precision and comprehensiveness of analyzing the root causes of fractures, facilitating the classification of different crack types (Aliabadian et al. 2019, 2021;

Sharafisafa et al. 2018, 2019). Furthermore, such vectors have been extensively validated in investigating the mechanisms of crack coalescence (Fan et al. 2021; Zhang et al. 2021, 2022). The principle underlying the capability of DIC technology to capture the intricate variations in displacement vectors across the surface of a specimen is illustrated in Fig. 5 (Dong et al. 2023).

Specifically, the digital speckle pattern image of the object before deformation is used as the reference image, and point p is marked as the recognized speckle point. As external forces deform the specimen, the position of the speckle point changes, resulting in point p to be displaced horizontally along the x-axis by u and vertically along the y-axis by v, eventually arriving at a new position p'. The changes in these displacement vectors can be captured and recorded by DIC technology. Therefore, DIC has emerged as a crucial tool for analyzing the alterations in displacement vectors during crack evolution (Han et al. 2022; Munoz et al. 2016; Wang et al. 2023a). The displacement vectors can accurately reveal the crack initiation mechanism and determine its type, which has been widely applied and validated in crack evolution mechanism research (Wang et al. 2023b).
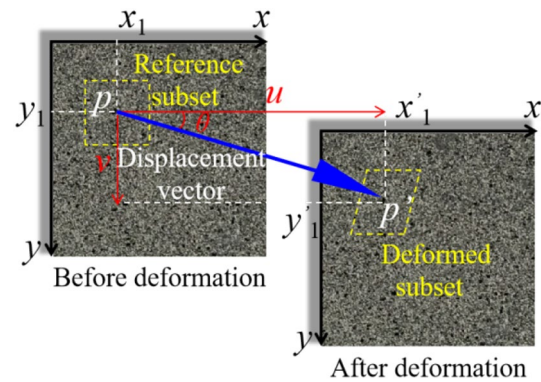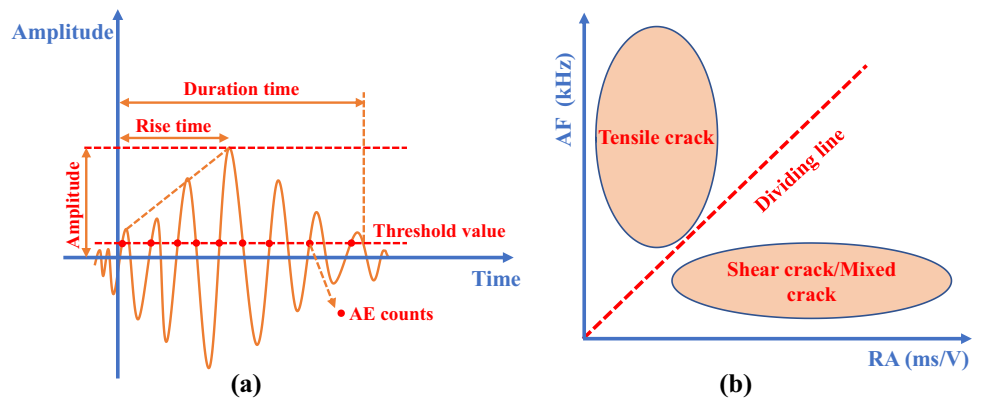

Fig. 5 Schematic diagram of the basic principle of displacement vectors based on DIC

Fig. 4 Physical meaning of AE waveform parameters and crack division diagram: **a** AE waveform parameters; **b** crack classification

Using the Vic-2D software, surface speckle pattern data of the specimen during the test were recorded, which included the coordinates and displacement values of the speckle points along the axes. Vector analysis was then performed on the raw data to calculate the amplitude and direction of the displacement vector of each speckle point on the specimen surface, using the following formula:

$$l = \sqrt{u^2 + v^2}, \tag{3}$$

$$\theta = \frac{180}{\pi} \times \arccos \frac{u}{l}, \tag{4}$$

where u and v represent the displacement distances of the speckle points along the x-axis and y-axis, respectively, l represents the displacement distance of the speckle points, and θ represents the angle between the displacement vector of the speckle point and the positive x-axis.

Through the application of vector analysis on the raw data acquired via Vic-2D software, researchers can precisely determine the displacement vectors of speckle points on the specimen surface. To accurately determine whether crack coalescence was controlled by tension, shear, or a combination of both, the amplitude and directional data of the displacement vectors were visualized using Origin 2020 software. The collection of displacement vectors of small units on the specimen surface constitutes a displacement field, which can be used to intuitively determine the characteristics of the displacement field and analyze the crack evolution mechanism. The initial state of the displacement field was assumed to be uniform and continuous, with all displacement vectors pointing in the same direction and linearly varying in size. However, during the crack coalescence process, the displacement vectors near the crack may suddenly change. For a more intuitive depiction of abrupt shifts in displacement vectors, Zhang and Wong (2014) summarized three patterns based on Displacement Trend Lines (DTLs), as shown in Fig. 6. The divergence of the relative DTLs at the fracture location signifies tensile displacement, corresponding to tensile failure (Fig. 6a). The convergence of the relative DTLs at the fracture location signifies shear displacement, corresponding to shear failure (Fig. 6c). In addition, there are also combined tensile and shear characteristics, which can be considered as a tensile-shear mixed failure mode (Fig. 6b).

The influence on displacement vectors stems from various factors, with the geometric configuration of flaws emerging as a primary determinant for distinct displacement vector manifestations (Zhang and Wong 2014). Throughout the process of crack coalescence, these displacement vectors might undergo alterations. However, relying solely on DTLs to delineate these vectors proves fundamental yet insufficient, particularly when confronted with intricate failure mechanisms and
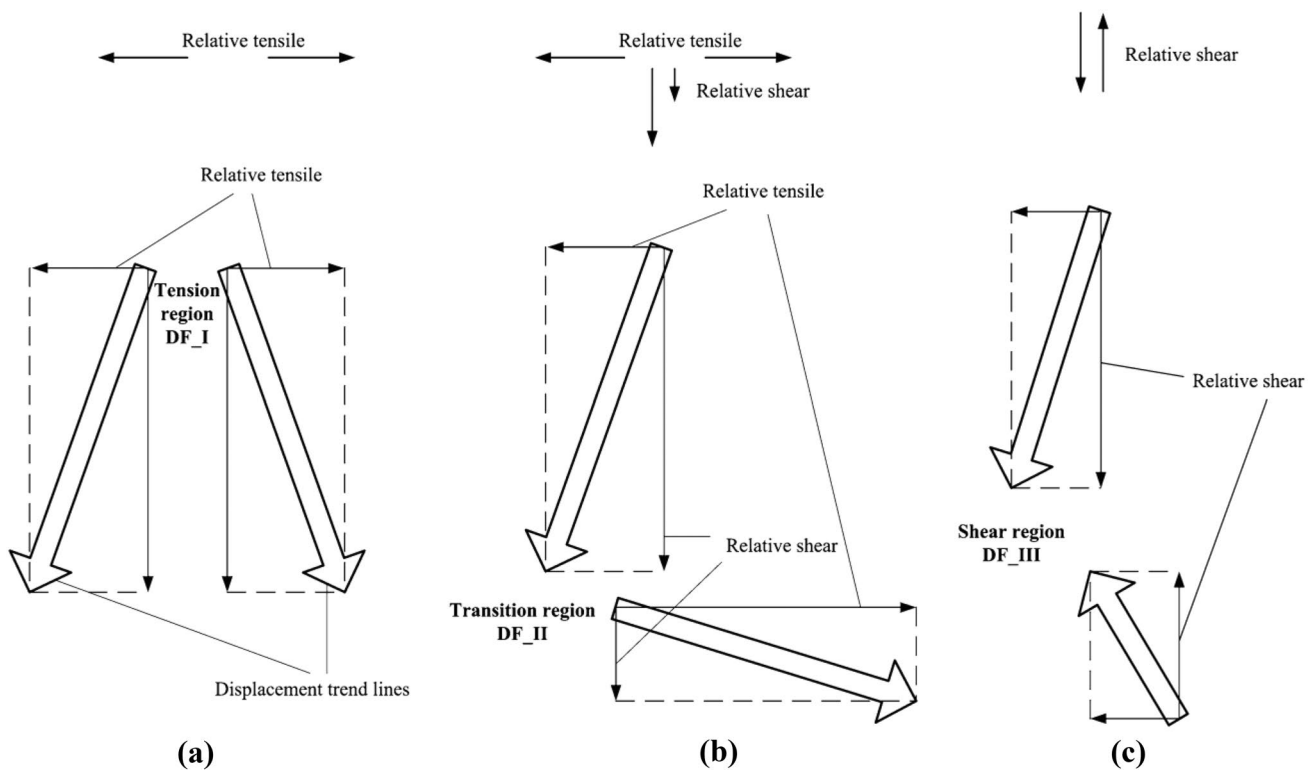

Fig. 6 Three displacement vector types defined by displacement trend lines (Zhang and Wong. 2014)

diverse crack types. This leads to a limited understanding of the failure mechanisms and crack types in certain cases, and more detailed analysis is needed. To address this limitation, a comprehensive analysis method termed divided displacement trend lines (DDTL) is proposed. This method involves classifying and defining the changes in displacement trend lines on both sides of the crack in detail. Taking a small crack element as an example, the schematic diagram is shown in Fig. 7a. There are two displacement trend lines on each side of the crack, randomly distributed in four equally divided regions. The displacement trend lines are divided into those pointing towards and away from the center. The divided displacement trend line is used to define the displacement types, which is illustrated in Fig. 7b. Absolute tensile or shear displacement lines are those perpendicular or parallel to the crack, irrespective of their size, but moving in opposite directions. Relative tensile or shear displacement lines are those that are perpendicular or parallel to the crack and in the same direction, where one is larger than the other. Parallel tensile or shear displacement lines are those of equal magnitude and in the same direction. Figure 7c illustrates a special case where the movement is in opposite directions. The movement in the crack direction is still classified as shear displacement, while the direction perpendicular to the crack, is a compressive displacement. It is widely recognized that rock has high compressive strength, and it is unlikely that pure compressive displacement would cause crack coalescence (Wong and Einstein 2009; Niu et al. 2019). It should be noted that pure compressive displacement within rock is infrequent. In contrast, shear-compression displacement is prevalent, particularly during the crack initiation stage. Following crack initiation caused by shear-compression displacement, the displacement vector gradually evolves into other types.

Various combinations of DDTL were derived, eliminating repeated and evidently incapable combinations that fail to induce crack propagation. The classification principle is based on a form of the components, as illustrated in Fig. 8.
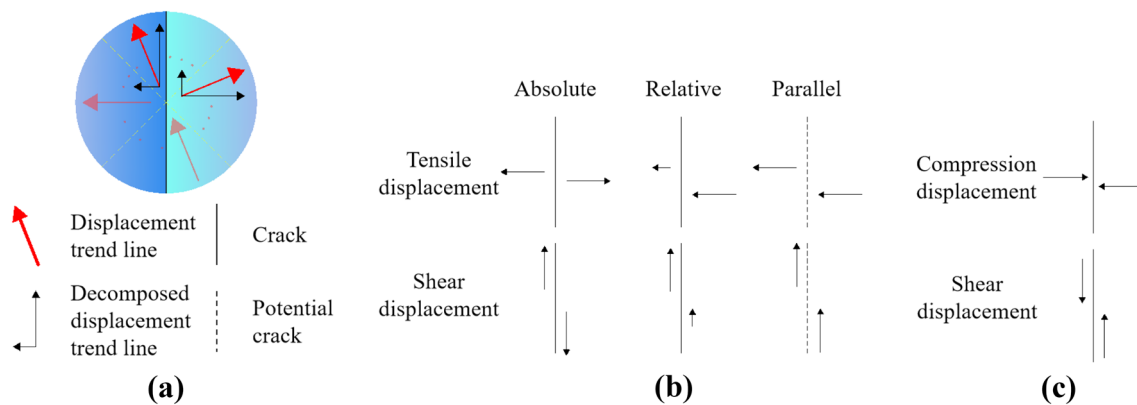
For example, the DDTL of tensile displacement is formed by combining the absolute tensile displacement component and the parallel tensile displacement component. Six types of DDTL that directly cause crack propagation were further categorized into subtypes, including tensile displacement, tensile-dominant displacement (Fig. 8a), shear displacement, shear-dominant displacement, shear compression displacement (Fig. 8b), and mixed displacement (Fig. 8c). It is noteworthy that mixed displacement is a combination of the relative displacement component and the parallel displacement component, representing an excessive phase of mixed tensile or mixed shear displacement. Additionally, detailed types of compression and uniform displacement vectors were listed, as depicted in Fig. 9. These types do not directly cause crack coalescence but appear before crack initiation or after coalescence. They are forms that indirectly contribute to crack coalescence.

3.3 Description of Crack Influencing Factors (CIF) Model

In the realm of linear elastic fracture mechanics (LEFM), it is a well-established principle that cracks can be classified into three primary modes based on the assumption of linear elasticity. These modes include opening mode (mode I), sliding mode (mode II), and anti-plane shear mode (mode III) (Irwin. 1957; Wang et al. 2021). The basic crack deformation modes of I and II are illustrated in Fig. 10 (Liu et al. 2021; Nikolic and Ibrahimbegovic. 2015). Mode I cracks occur when the tensile stress surpasses the material strength, resulting in an opening displacement that is perpendicular to the crack surface, as depicted in Fig. 10a. On the other hand, mode II cracks occur when the shear stress exceeds the material strength, resulting in a relative sliding parallel to the shear direction, as illustrated in Fig. 10b (Irwin. 1957; Xie et al. 2023). As for mode III cracks, this study does not

Fig. 7 Schematic diagram of divided displacement trend lines and decomposed displacement

Fig. 8 Displacement vector types defined by divided displacement trend lines: **a** tensile type displacement; **b** shear type displacement; **c** mixed type displacement
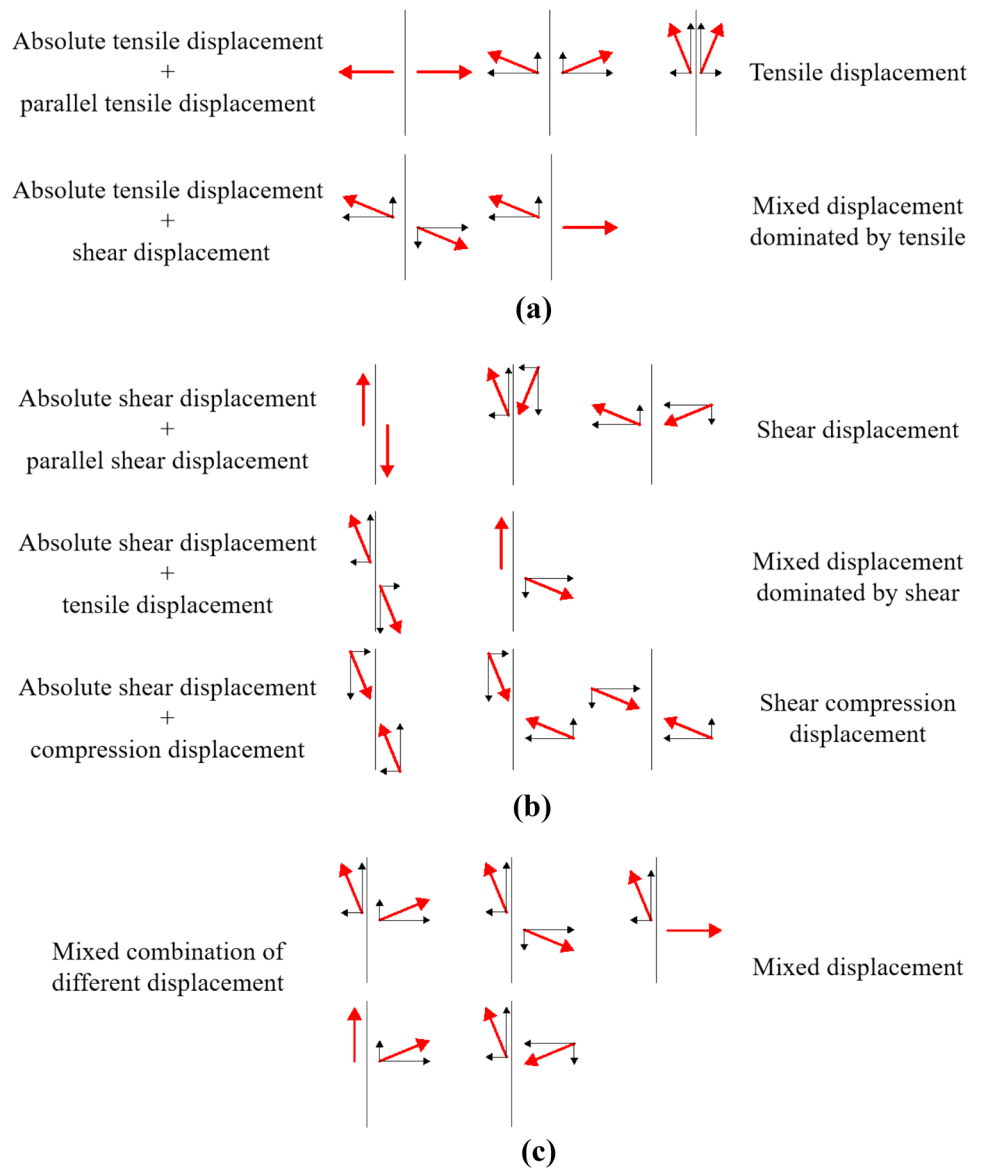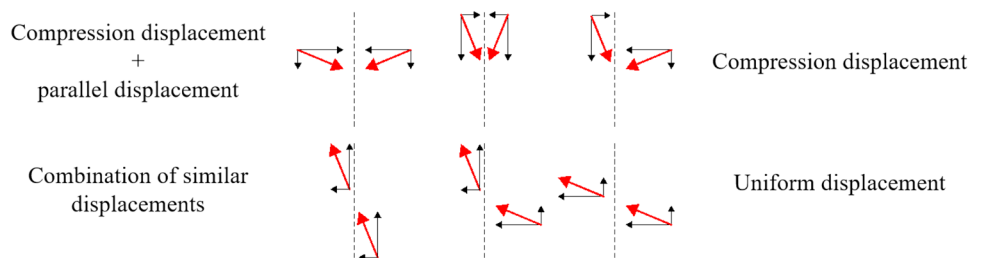
Absolute tensile displacement
+
parallel tensile displacement

Tensile displacement

Absolute tensile displacement
+
shear displacement

Mixed displacement dominated by tensile

(a)

Absolute shear displacement
+
parallel shear displacement

Shear displacement

Absolute shear displacement
+
tensile displacement

Mixed displacement dominated by shear

Absolute shear displacement
+
compression displacement

Shear compression displacement

(b)

Mixed combination of different displacement

Mixed displacement

(c)

Fig. 9 Two types of displacement vectors indirectly causing crack coalescence

Compression displacement
+
parallel displacement

Compression displacement

Combination of similar displacements

Uniform displacement

examine them due to the limitation of the Vic-2D software for investigating three-dimensional displacements.

Discerning between different types of cracks relies heavily on disparities in displacement patterns on either side of a crack. Tensile cracks exhibit an opening displacement, while shear cracks exhibit relative sliding. The displacement on

both sides of the crack can be characterized by monitoring point displacement, which can be obtained through DIC monitoring technology. Figure 10 illustrates monitoring points p_1 and p_2 on either side of the crack with an initial distance of l. The coalescence of the crack causes the monitoring points to be displaced to p_1' and p_2' with
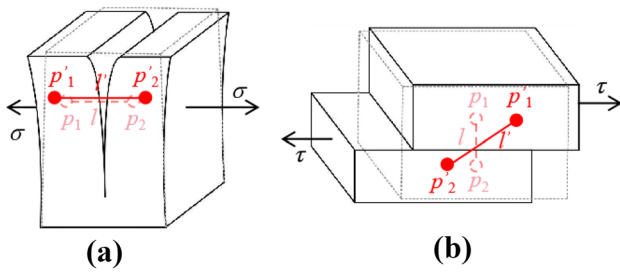
Fig. 10 Basic crack deformation modes: **a** mode I (opening mode); **b** mode II (sliding mode) (Liu et al. 2021)

a distance of l' after deformation. For the strain caused by different displacement models, two terms are introduced: the displacement difference of monitoring points caused by tensile strain D_t and caused by shear strain D_s. Based on the displacement pattern on both sides of the crack, the crack influencing factors (CIF) calculation model is established. The CIF calculation model is a quantitative approach for calculating the factors that impact crack coalescence. This model provides a means to quantify the impact of tensile and shear displacements on crack coalescence across various locations and time intervals. This model can be used to analyze the crack initiation and propagation process and to identify the type of crack.

The complexity of the displacement difference in monitoring points induced by tensile or shear stress arises from multiple influencing factors. The analysis of different scenarios and the consideration of various effects can lead to a more accurate and comprehensive understanding of the displacement difference of monitoring points. To facilitate the explanation of the calculation principles, the displacement of monitoring points is systematically classified into four cases, ranging from simple to complex, as shown in Fig. 11. These cases are: monitoring points with the same displacement (Fig. 11a), monitoring points with the same vertical displacement (Fig. 11b), monitoring points with different vertical and horizontal displacements (Fig. 11c), and monitoring points with different initial

horizontal positions and displacements (Fig. 11d). The angle between the line connecting the monitoring points and the horizontal direction is denoted by θ, and the angle between the line connecting the monitoring points after displacement and the horizontal direction is denoted by θ'.

For the previous two cases, the D_t is relatively simple, and can be expressed as Eq. (5):

$$D_t = l' - l = u_2 - u_1, \tag{5}$$

where u_1 represents the horizontal displacement of monitoring point p_1, u_2 represents the horizontal displacement of monitoring point p_2.

However, the latter two cases are more complex and are more representative of actual scenarios. By analyzing the geometric relationship shown in Fig. 11c, the horizontal displacement difference of monitoring points can be expressed as Eq. (6), and the D_t can be expressed as Eqs. (7) and (8).

$$l'\cos\theta' - l = u_2 - u_1, \tag{6}$$

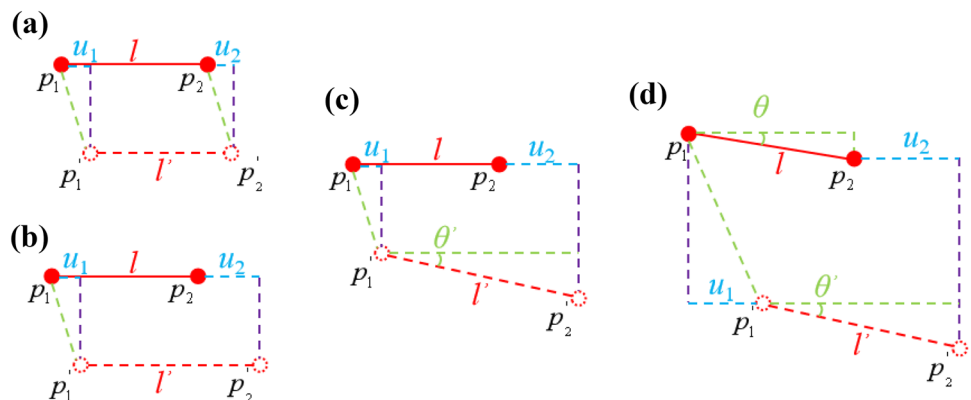$$D_t = l' - l = l'(1 - \cos\theta') + (u_2 - u_1), \tag{7}$$

$$D_t = l' - l = \frac{(u_2 - u_1) + l}{\cos\theta'} - l. \tag{8}$$

Based on the similarity of geometric relationships, the horizontal displacement difference of monitoring points can be expressed as Eq. (9), the D_t can be expressed by Eqs. (10) and (11) through the analysis of the displacement relationship shown in Fig. 11d.

$$l'\cos\theta' - l\cos\theta = u_2 - u_1, \tag{9}$$

$$D_t = l' - l = \frac{l'(\cos\theta - \cos\theta') + (u_2 - u_1)}{\cos\theta}, \tag{10}$$

Fig. 11 Principle diagram of tensile displacement analysis of monitoring points

$$D_t = l\prime - l = \frac{(u_2 - u_1) + l\cos\theta}{\cos\theta\prime} - l. \tag{11}$$

Considering that the monitoring point connection line is parallel to the horizontal direction during the initial setup, the above equation can be simplified to Eqs. (12) and (13).

$$D_t = l\prime - l = l\prime(1 - \cos\theta\prime) + (u_2 - u_1), \tag{12}$$

$$D_t = l\prime - l = \frac{(u_2 - u_1) + l(1 - \cos\theta\prime)}{\cos\theta\prime}. \tag{13}$$

Compared with the displacement of the monitoring point caused by tensile, the displacement caused by shear is slightly more complicated, as shown in Fig. 12. Assuming that the change in the distance between monitoring points is completely caused by shear displacement, denoted by w_{xy}, the angle between the crack and the horizontal direction is denoted by φ.

As shown in Fig. 12a, the monitoring points slide in the opposite direction. The geometric relationship of the displacement displays that the angle γ between the shear displacement and the horizontal direction is shown in Eq. (14).

$$\gamma = \arccos\left(\frac{u}{w_{xy}}\right). \tag{14}$$

The displacement component m_1 of the shear displacement in the crack expansion direction is shown in Eq. (15).

$$m_1 = \cos(\gamma_1 - \phi)w_{xy1}. \tag{15}$$

Even though the monitoring points are moving in the same direction, as shown in Fig. 12b. The above geometric relationship still holds. The displacement difference along the crack shear strain direction at the monitoring point, which is the D_s, is shown in Eq. (16).

$$D_s = m_1 - m_2 = \cos(\phi - \gamma_1)w_{xy1} - \cos(\phi - \gamma_2)w_{xy2}. \tag{16}$$

In conclusion, it is imperative to acknowledge that, in the majority of real-world scenarios, the displacement difference observed in monitoring points results from a combination of both tensile and shear forces. Since rock is a collection of minerals, the shear fracture surface cannot be smooth. As a result, the shear between cracks will produce shear dilation or shear contraction effects. Microscopically, there exists not only shear displacement but also tensile and compressive displacement between monitoring points. As shown in Fig. 13a, assuming that the monitoring point displacement dominated by shear failure is caused by shear displacement followed by tensile displacement. Initially, point p_2 undergoes translation to q_1, followed by further movement to q_2 due to shear displacement, and ultimately arrives at p_2' after experiencing tensile displacement. The q_1q_2 is the theoretical shear displacement. One representative case is shown in Fig. 13b. The larger rotation angle of the monitoring point line is created by the effect of shear displacement. Notably, the vertical displacement disparity between the two monitoring points exceeds the anticipated

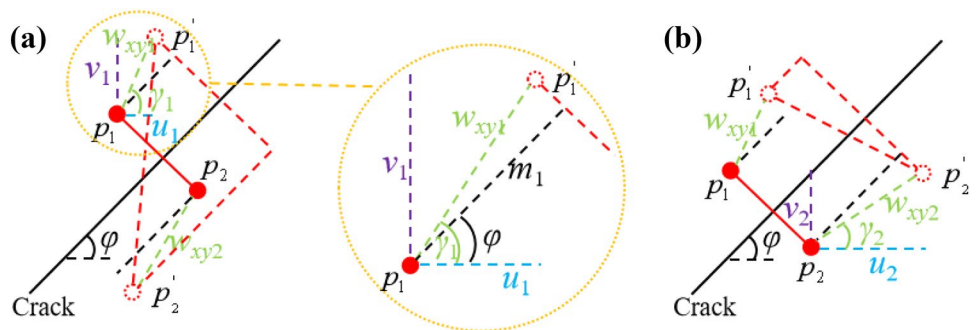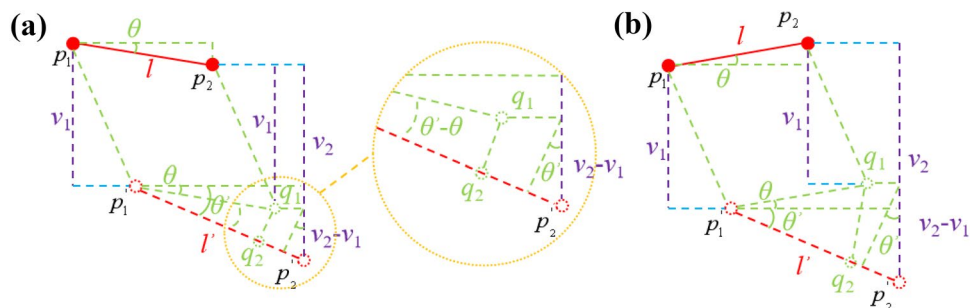Fig. 12 Principle diagram of shear displacement analysis of monitoring points

Fig. 13 Principle diagram of shear dilation displacement analysis of monitoring points

theoretical shear displacement. The reason is that there is not only the displacement generated by shear but also the displacement generated by shear dilation or shear contraction effects.

The aforementioned analysis reveals the presence of both tensile and shear displacements in the monitoring points surrounding the crack when observed from a microscopic perspective. Crack coalescence is the result of a combination of tensile and shear strains in multiple directions, rather than being solely controlled by either tensile or shear displacement. Even when both forms of displacement coexist concurrently, there is invariably a dominant type, and their relative proportions vary over time. This affects the initiation time, geometric shape, and propagation path of the initiated crack, ultimately influencing the failure mode and mechanical properties of the specimen. Traditionally, the classification of crack types has predominantly relied on the moment of crack coalescence and the characteristics post-coalescence. The situation before coalescence has not been effectively studied. Therefore, it is necessary to quantify the entire process of crack coalescence, and then determine the main control factors affecting crack coalescence.

Since the displacement difference caused by tensile displacement at the monitoring point is significantly exceeds that caused by shear displacement, it is not feasible to perform direct calculations on the two datasets. The displacement data obtained from the monitoring points are normalized using Eq. (17):

$$D^* = \frac{D - \min D}{\max D - \min D},\tag{17}$$

where D^* represents the displacement difference after normalization, and D represents the displacement difference at the monitoring point due to tension or shear.

As previously elucidated, the discrepancy in displacement observed in monitoring points is attributed to both tensile and shear forces, resulting in a comprehensive data set of D_t and D_s values. By meticulously comparing normalized data before and after crack coalescence from the same set of monitoring points, the predominant influence of either tensile or shear factors during crack coalescence can be accurately ascertained for each region. This analytical approach allows for a more profound understanding of the mechanics governing crack coalescence phenomena. Building upon the above theoretical derivation, the CIF calculation model is introduced to quantify the dominant factor of crack coalescence, and the formula is shown in Eq. (18)

$$\text{CIF} = \lg \frac{D_t^*}{D_s^*}.\tag{18}$$

3.4 Application of the Methodology

Specimen S-0-1 serves as an exemplary demonstration of model utilization, and the methodology flow is shown in Fig. 14. The AF-RA model, relying on AE data, assesses the percentage of different types of microcracks within the specimen from a microscopic perspective. Conversely, the DDTL model scrutinizes the variation in displacement trends caused by cracks from a macroscopic standpoint. Lastly, the CIF model registers the variation of dominant factors governing crack coalescence throughout the entire testing process. Varied forms of crack coalescence affect the results of the aforementioned three models, from which the crack coalescence mechanism can be analyzed and type can be determined.

The CIF, being an innovative model, deserves a comprehensive description of its computational steps. Detailed steps of the CIF model are shown in Fig. 14. Initially, the location of the crack is determined from the displacement field image. The crack is divided into three distinct sections, namely, the initial section (1), the intermediate section (2), and the terminal section (3). Data monitoring points are meticulously positioned at the center of each crack section, maintaining a distance of 1.5 mm from the crack on both sides through the input of coordinate parameters. Subsequently, the software diligently summarizes the data from each of these points. The crucial monitoring point data is efficiently collected using the Vic-2D software. This step is conducted using comprehensive statistical methods, further reinforcing the accuracy of the acquired data. Finally, upon successful completion of the data gathering, the valuable data is thoughtfully organized and elegantly presented in a structured data table.

4 Experimental Results

4.1 Stress–Strain Curves and AE Characteristics of the Specimen

The stress–strain curves, AE signals, and crack images for rock specimens are shown in Fig. 15. The results reveal significant differences in the effects of flaw width and inclination on specimen damage. The stress–strain curve of the specimen can be divided into pore closure stage, elastic deformation stage, yielding stage and post-peak stage. A corresponding correlation between AE signals and crack formation is observed, where macroscopic crack initiation, propagation, and coalescence coincide with the appearance of relevant AE signals. Specifically, when the length and width of the flaws remain constant, the compressive strength of the specimen increases with the increase of flaw

Fig. 14 Methodology flowchart for studying crack coalescence mechanism and crack types determination
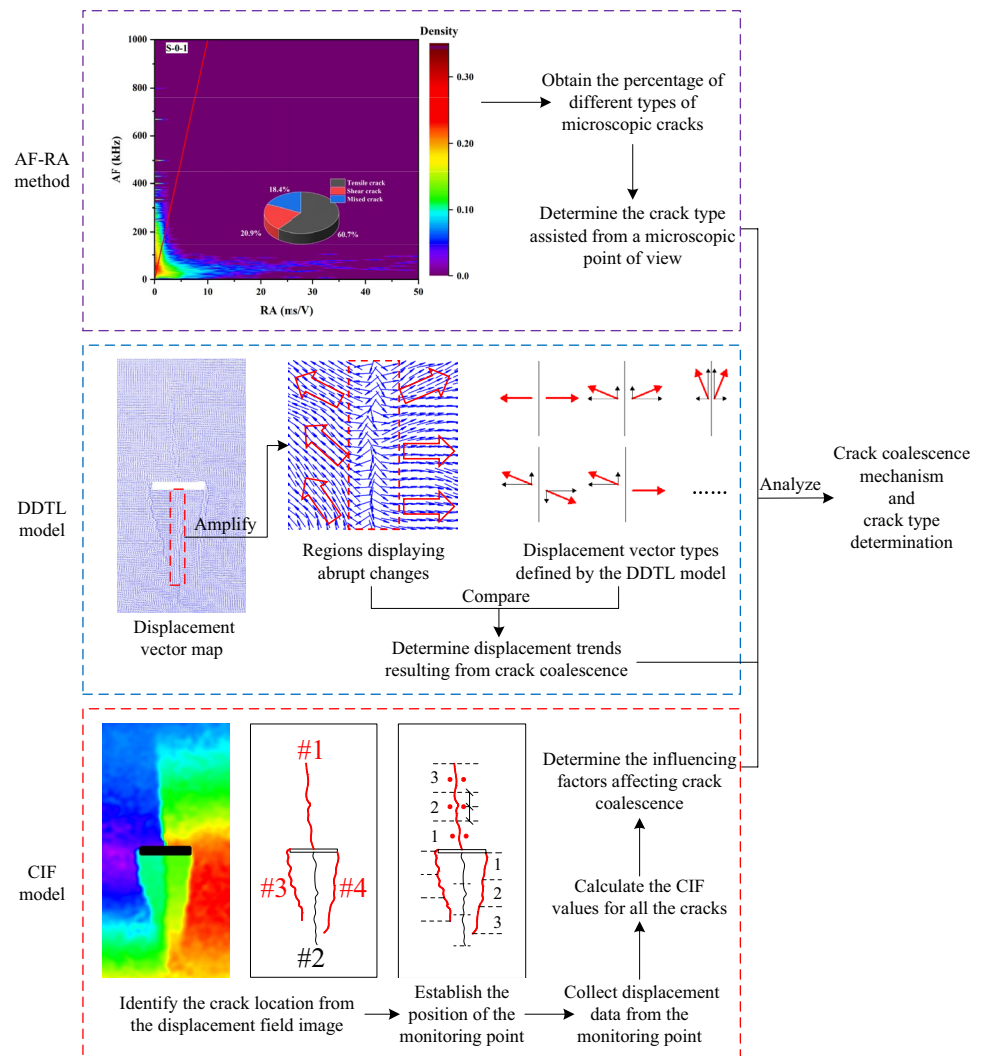
inclination angle. Compared to the specimens with other inclinations, the specimens with a flaw inclination of 90° did not have a significant yielding phase before peak compressive strength. Under condition of constant flaw length and inclination angle, the phenomenon of crack coalescence in the specimen prominently rises with the increase of flaw width. Crack initiation and coalescence are more likely to occur in specimens with small flaw widths, while crack coalescence is relatively lagging in specimens with large flaw widths.

4.2 Crack Type Determination Based on the AE

Figure 16 illustrates the crack distribution and kernel density estimation (KDE) results of the specimens based on their AF and RA values. The pie chart illustrates that tensile cracks dominate during the loading process, with their proportion escalating alongside the flaw angle. Conversely, the proportion of shear cracks decreases with the angle of the flaw. Additionally, the proportion of tensile cracks decreases with increasing flaw width, while the proportion of mixed cracks increases. The density cloud map reveals that high-density AE events are concentrated in the area of tensile cracks, further indicating the dominance of tensile fracture in the specimen. The AF value distribution range for specimens of varying angles and widths remains relatively consistent, primarily ranging between 0 and 250 kHz. The RA value distribution concentrates within the 0–20 ms/V range, but this range decreases with increasing flaw angle and increases with increasing flaw width. As the flaw inclination increases, the high-density area of AF and RA scattered points gradually approaches the AF axis, which is consistent with the proportion of tensile cracks to flaw angle in the pie chart. The result provides a statistically based quantitative description of the different crack characteristics.
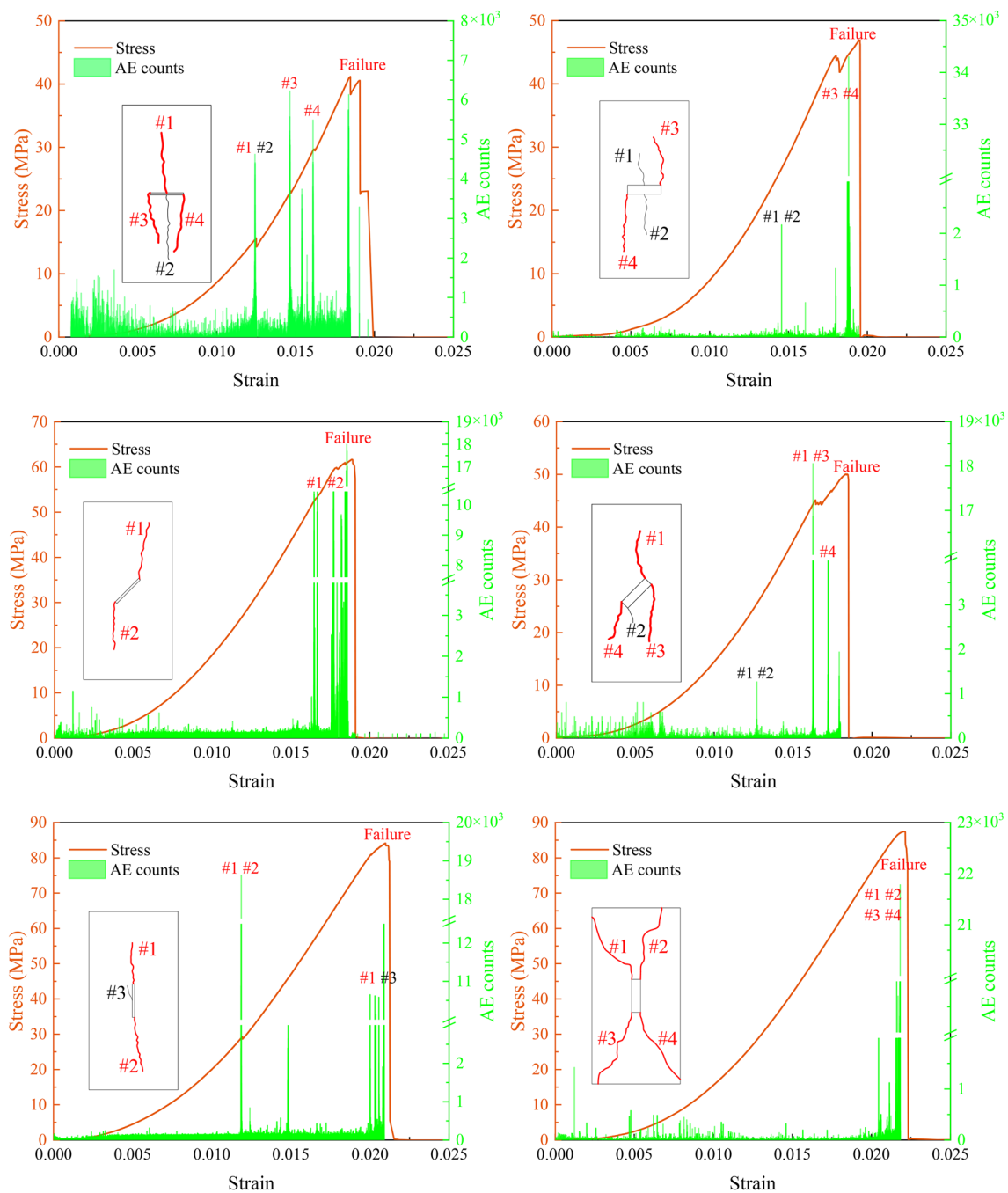
Fig. 15 Stress–strain curves, AE signals and crack images of rock specimens

4.3 Crack Type Determination Based on the Displacement Vector

The analysis of the displacement vectors of cracks in different sections can provide insights into the crack propagation patterns and the resulting failure mechanisms. The presented displacement vectors, depicted in Figs. 17, 18,19, 20, including enlarged images of critical positions and divided displacement trend lines. To categorize crack type, an analysis

of the initial section 1, intermediate section 2, and terminal section 3 of different cracks was conducted, considering the trend lines of displacement vectors on both sides of the crack.

Figure 17a is a schematic illustration of the S-0-1 crack distribution. Figure 17b shows the displacement vectors of the three cracks in S-0-1 and analyzes cracks #2 and #3. The displacement vector around the periphery of crack #2 moves backward almost perpendicularly to the direction
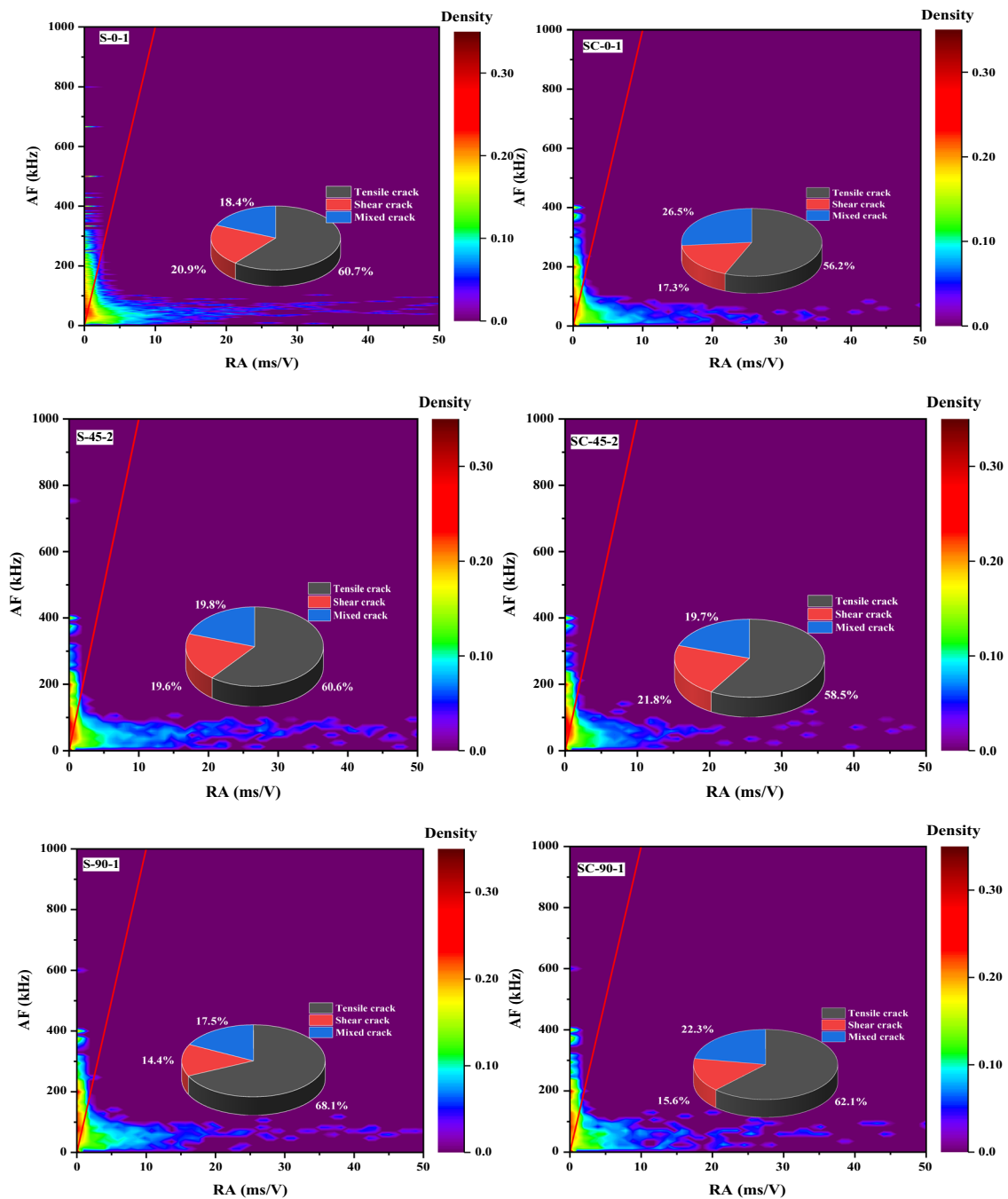
Fig. 16 Kernel density estimation and crack division of discrete points of AF and RA

of the crack (Fig. 17c). The dominating trend line of the displacement vector component perpendicular to the crack is evident (Fig. 17d), signifying that the crack has separated and fractured on both sides, characterizing it as a pure tensile crack (*T*). From Fig. 17e, it can be observed that there is a trend of inward compression in the displacement vectors surrounding crack #3. This results in shear displacement along the vertical direction in addition to the tensile

displacement along the horizontal direction of the crack (Fig. 17f). The formation mechanism of crack #3 was analyzed based on the extension process. Firstly, the crack displayed tensile displacement during the initiation phase. Subsequently, owing to the aggregation of the preceding crack #2, the surrounding rock blocks moved outward. The displacement of crack #3 was affected by the movement of the rock blocks, resulting in shear displacement. Therefore,
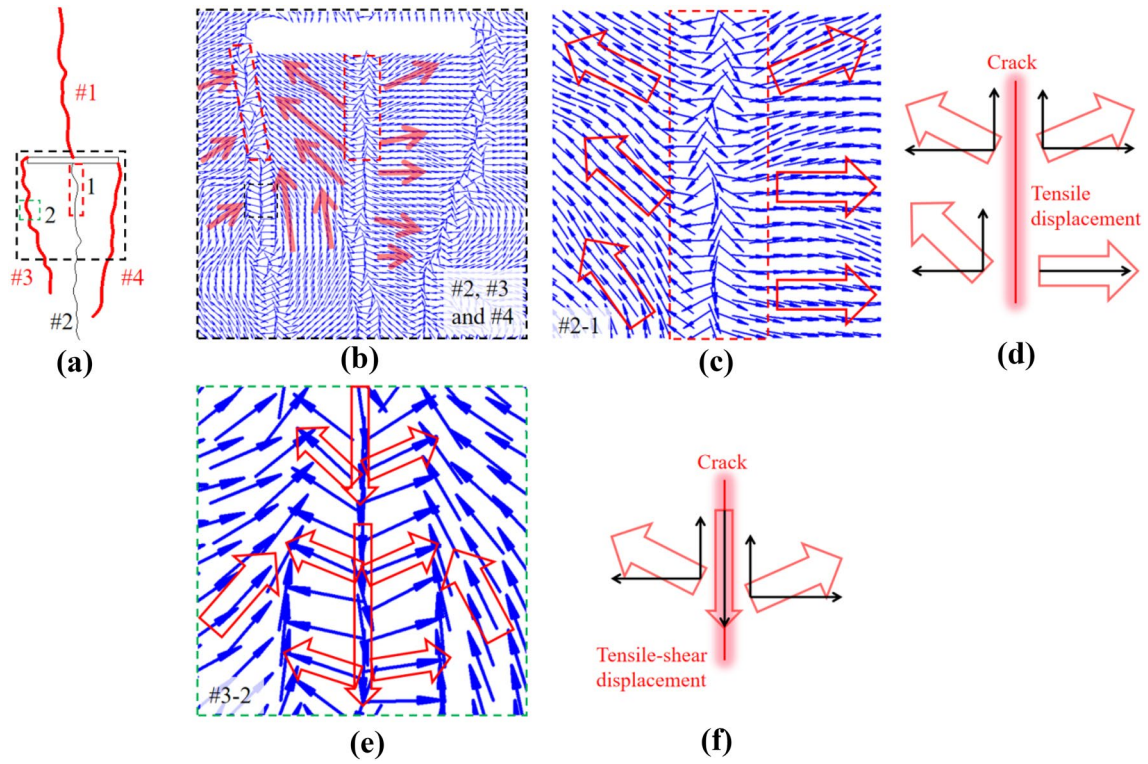
Fig. 17 Enlarged images and divided displacement trend lines of the S-0-1 cracks
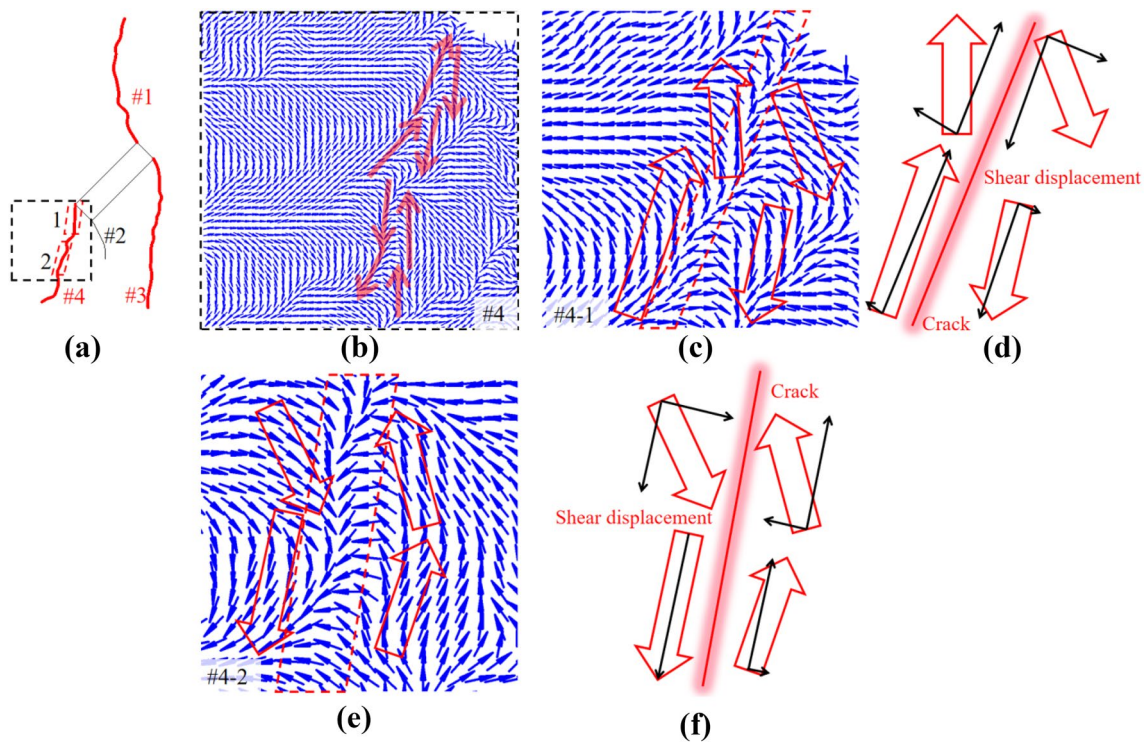

Fig. 18 Enlarged images and divided displacement trend lines of the SC-45-2 #4 crack
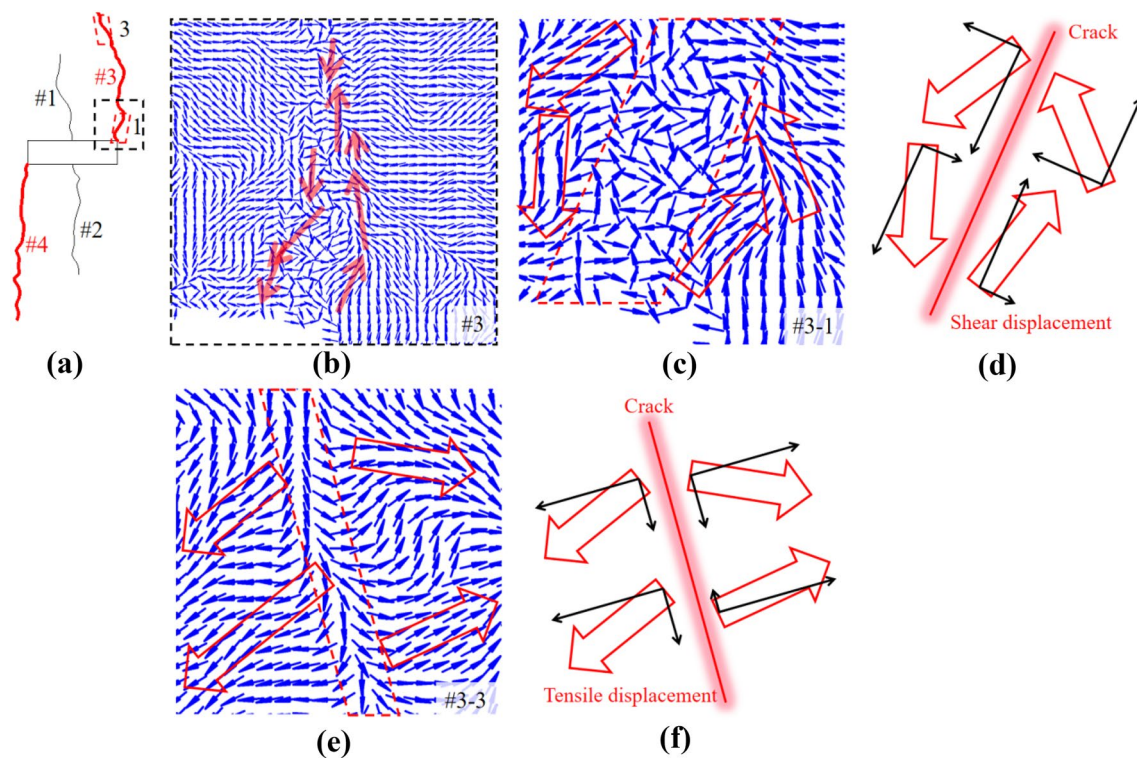
Fig. 19 Enlarged images and divided displacement trend lines of the SC-0-1 #3 crack

crack #3 is a mixed crack, defined as a tensile-shear crack (TS).

Figure 18a depicts the distribution of the SC-45-2 crack. In Fig. 18b, the displacement vectors of crack #4 are displayed, with the initial section #4-1 and intermediate section #4-2 analyzed. Figure 18c, e illustrates that the displacement vectors at the periphery of crack #4 move away from the crack in a direction almost parallel to it. The divided displacement trend line parallel to the crack dominates (Fig. 18d, f) indicating shear sliding on both sides of the crack. This is identified as a pure shear crack, defined as a shear crack (S).

Figure 19a depicts the distribution of SC-0-1 cracks. It is noteworthy that different types of displacement are observed at two sections of crack #3, as shown in Fig. 19c, e, which are the initial section #3-1 and terminal section #3-3, respectively. Figure 19c illustrates the displacement vector at the terminal section of crack #3-1, which moves almost parallel to the direction of the crack. The dominant component of the displacement trend line is parallel to the crack (Fig. 19d), indicating shear slip on both sides of the crack. However, as the crack propagates in the vertical direction, the displacement vector exhibits a deflection. Figure 19e shows that the displacement vector at the terminal section of crack #3-3 moves backwards almost

perpendicular to the crack, and the dominant component of the displacement trend line is perpendicular to the crack (Fig. 19f), indicating that both sides of the crack are fractured and separated. This is a combined crack, defined as a shear-tensile crack (ST).

Figure 20a depicts the distribution of SC-45-2 cracks. Figure 20b–d shows the displacement vectors of SC-45-2 crack #3 at different times, analyzing the initial section #3-1. Figure 20b reveals a distinctive feature of compressive shear displacement around the crack during its initiation. Figure 20c shows the displacement field around the crack during propagation, where the compressive displacement previously observed shifts towards a shear displacement. Subsequently, in Fig. 20d, during coalescence, a shift to tensile displacement becomes evident along the crack. From these observations, it is inferred that the genesis of crack #3 initiates with the emergence of compressive shear displacement at the tip of the flaw. As the compressive deformation cannot be sustained, the displacement at the flaw tip shifts towards a shear displacement. The absence of transverse enclosing pressure creates conditions conducive to the tensile expansion of the crack. Ultimately, this leads to outward tensile displacement. This is a type of compound crack where shear is the dominant factor in the crack coalescence, and therefore is defined as a shear-tensile crack (ST).
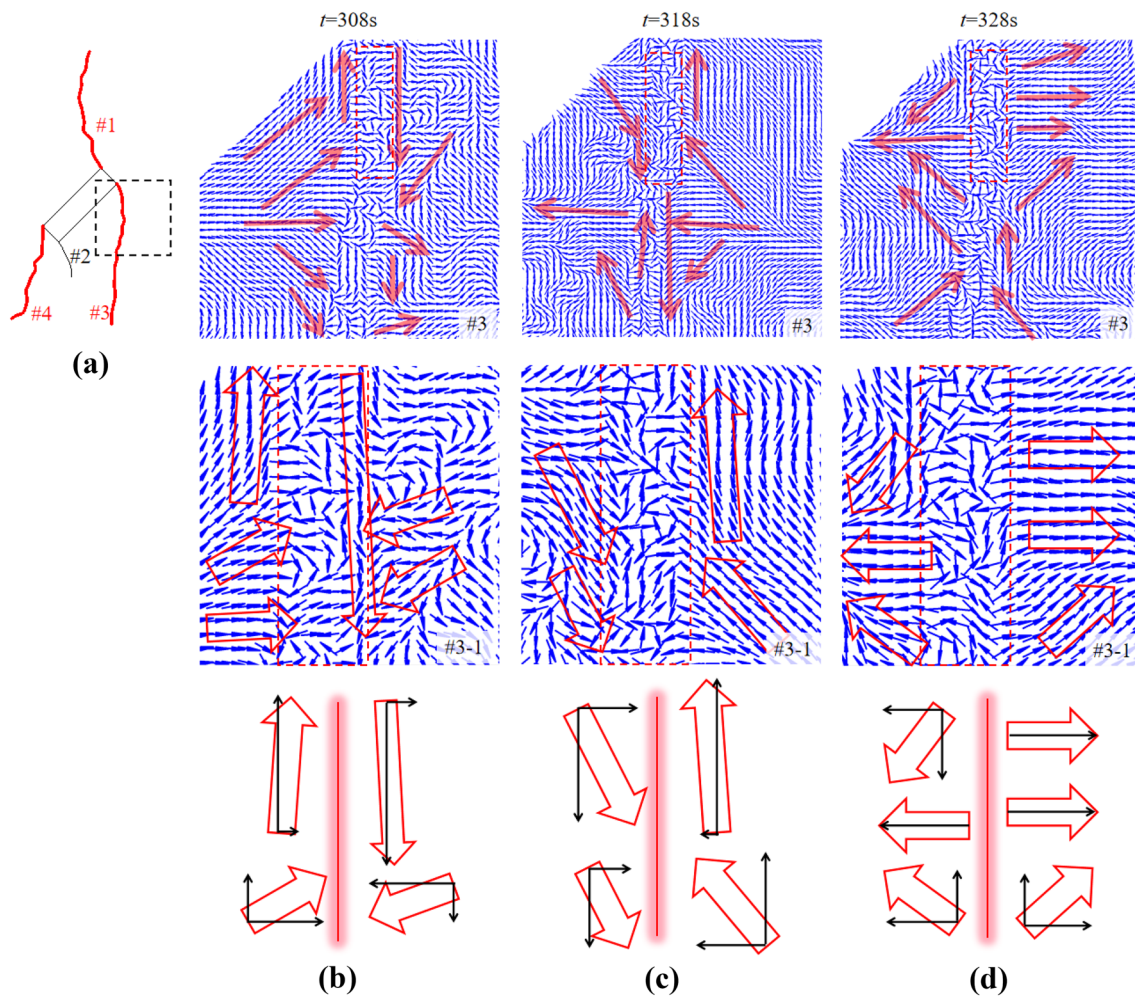
Fig. 20 Enlarged images and divided displacement trend lines of the SC-45-2 #3 crack

4.4 Crack Type Determination Based on the DIC

A crack determination model based on DIC monitoring data was employed to generate the CIF curve maps for various cracks, as shown in Figs. 21, 22, 23, 24, 25. The physical meaning of the curve is as follows: CIF > 0 indicates that tensile stress is the dominant factor, while CIF < 0 indicates that shear stress is the dominant factor, and the further away from 0, the greater the influence of tensile or shear stress. A descending trend in the curve signifies an increasing impact of shear stress or a diminishing effect of tensile stress, while an ascending trend indicates the opposite. To facilitate analysis, the process of crack coalescence is roughly divided into four stages based on the characteristics of the crack CIF curve: initiation stage (I), propagation stage (II), coalescence stage (III), and post coalescence stage (IV). The CIF curves are obtained separately for the three sections of the crack: initial section (CIF-1), intermediate section (CIF-2), and terminal section (CIF-3).
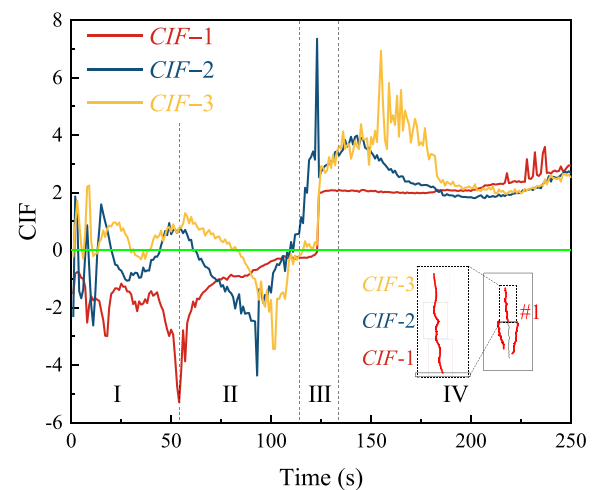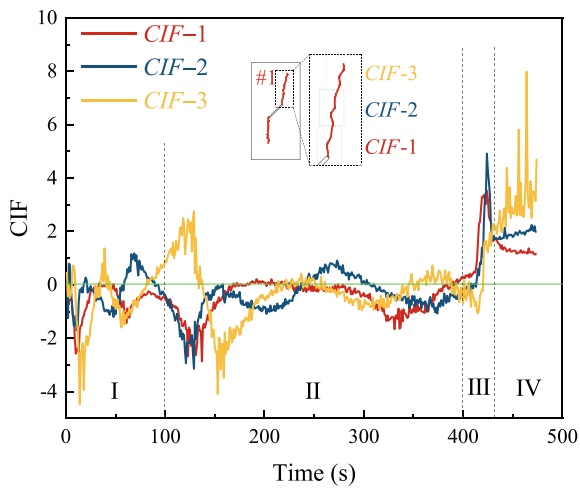

Fig. 21 CIF curve of specimen S-0-1 (#1 crack)
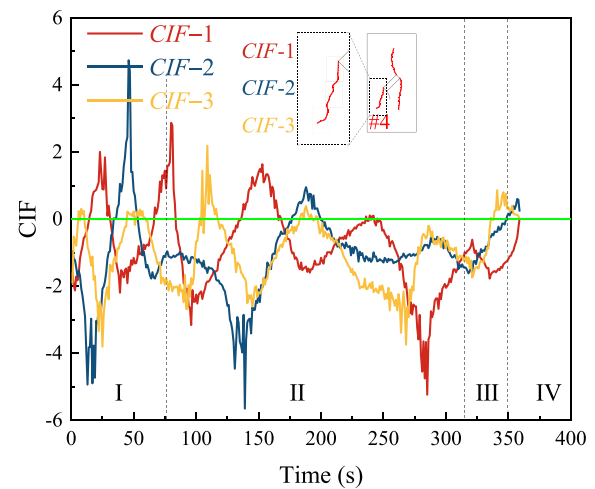
Fig. 22 CIF curve of specimen S-45-2 (#1 crack)

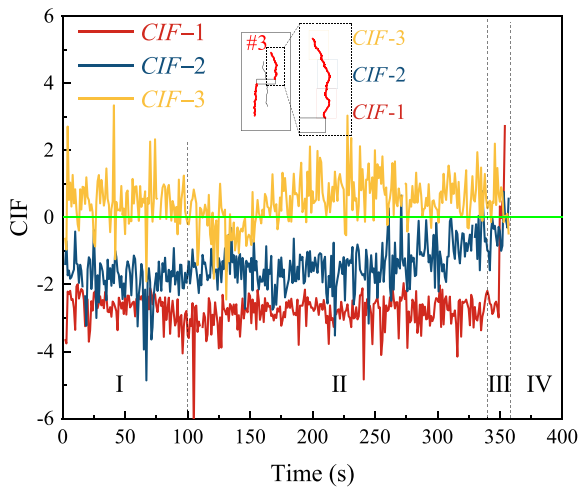**Fig. 23** CIF curve of specimen SC-0-1 (#3 crack)

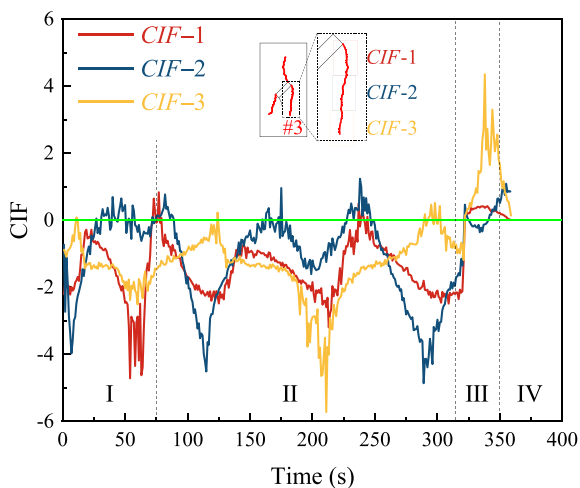**Fig. 24** CIF curve of specimen SC-45-2 (#3 crack)

Fig. 25 CIF curve of specimen SC-45-2 (#4 crack)

In Fig. 21, the CIF curve of crack #1 in specimen S-0-1 vividly illustrates the interplay of tension and shear during the crack coalescence process. The monitoring points of crack coalescence at the initiation stage are dominated by shear displacement, and the shear displacement of the crack initial section is significantly larger than other sections. After approximately 55 s, the influence of tension on the crack initial section gradually increases. And around 90 s, similar tension-related effects manifest in the intermediate and terminal sections, indicating the gradual extension of tension's influence from the initial section to the terminal section. Prior to crack coalescence, a remarkable rise in CIF values signifies the prevailing influence of tensile displacement driving the coalescence process. As crack coalescence approaches, there is a rapid and pronounced escalation in the CIF across the entire crack section. During the coalescence stage, the influence of tension on each section rapidly increases, and in the post coalescence stage, tension becomes the dominant factor for crack propagation. The crack can be classified as a T-type crack according to the above analysis.

Figure 22 presents the CIF curve of #1 crack in specimen S-45-2, which shows a relatively stable state in the propagation stage, with shear being the dominant factor, but its degree has significantly decreased compared to the early stage. Preceding crack coalescence, the CIF value remains constrained within the interval of −1 to 1, displaying no discernible increment. This observation suggests that both tensile and shear are synergistically reinforcing each other, indicating the absence of a dominant crack coalescence factor at this stage. During the crack coalescence, the influence of tension rapidly propagated

from the initial section to the terminal section, emphasizing tension as the dominant factor promoting crack coalescence and propagation. This crack is classified as TS-type.

Figure 23 shows the CIF curve of #3 crack in specimen SC-0-1. The CIF curve of this crack exhibits a distinct difference compared to other cracks. The crack initial and intermediate sections are mainly dominated by shear, while the terminal section is mainly dominated by tensile. Preceding crack coalescence, the CIF values exhibit no significant fluctuations, indicating that the factors affecting crack coalescence remain unchanged. The dominance of shear is most conspicuous near the flaw, and as the crack moves away from the flaw, tensile dominance gradually increases. This corresponds to the mixed crack type and initiation mechanism proposed by Wong and Einstein (2009). This crack is classified as ST-type.

Figure 24 shows the CIF curve of #3 crack in specimen SC-45-2. During the entire crack propagation process, shear dominates the displacement changes of the monitoring point for a long time. During the crack initiation stage, the strains within different parts of the crack lack coordination. As the propagation stage ensues, the initial and intermediate sections exhibit a combination of relative consistency and fluctuation. This reflects the complexity of shear-dominant strain. During the propagation stage, the influence of tensile stress increases significantly. Preceding crack coalescence, CIF values oscillate in waves within the range of -5 to 0, emphasizing shear as the dominant factor. As crack coalescence approaches, the CIF curve exhibits an upward trend with a relatively moderate final value, suggesting that tensile displacement assumes a secondary role in the process of crack coalescence. In the post coalescence stage, the influence of tensile stress on the intermediate and terminal sections is significantly higher than that on the initial section. This crack is classified as ST-type.

Figure 25 shows the CIF curve of #4 crack in specimen SC-45-2. In the initiation stage, the values of CIF fluctuate significantly, and the dominant factors fluctuate between tensile and shear. In the propagation stage, the fluctuation amplitude slightly decreases. Preceding crack coalescence, the CIF values consistently remain below 0, and the corresponding CIF curves exhibit no conspicuous upward trend. This observation strongly implies that shear serves as the primary driving crack coalescence. In the propagation and coalescence stage, the influence of shear stress is significantly greater than that of tensile stress. Throughout the propagation and coalescence stage, the influence of shear significantly outweighs that of tensile. Shear maintains dominance both in terms of control and time, and the final crack coalescence is not dominated by tensile. This crack is classified as S-type.

5 Discussion

5.1 Model Rationality Analysis

The determination of crack types based on the CIF model and the DDTL model are complementary methods. Figure 26 shows the results of the crack type determination methods used in this experiment for crack #2 in specimen S-0-1. The CIF model can introduce time variables for a quantitative study of crack types throughout the process (Fig. 26a). The DDTL model (Fig. 26b) and the maximum principal strain field obtained by DIC (Fig. 26c) provide visualization of the crack.

From the CIF curve (Figs. 21, 22, 23, 24, 25, 26), it is easy to observe that in both the initiation stage (I) and propagation stage (II), most cracks exhibit a characteristic of alternating tensile and shear displacements. Even for tensile cracks, shear displacement dominates in the initiation stage (I). The main reason for this phenomenon is that the monitoring points are connected in the horizontal direction in this experiment. Before the crack coalescence, the vertical (shear) displacement of the monitoring point is larger than the horizontal (tensile) displacement by the axial compressive stress. The vertical constraint on monitoring points leads to limited vertical displacement, while horizontal displacement is not restricted, resulting in a continuous transformation of the vertical displacement to horizontal displacement in some regions. The displacement vector at $t = 62$ s in Fig. 26b corroborates the rationality of the CIF curve for crack #2 in S-0-1, illustrating greater shear strain than tensile strain before the formation of a tensile crack. The trend lines of some displacement components in Fig. 26b show changes during the loading process, which verifies the reasonableness of the alternating tensile and shear strains before the crack coalescence shown in Fig. 26a.

The values of the CIF curve during the coalescence stage (III) represent one of the main criteria for crack type determination. At this stage, the CIF curve of a tensile crack rapidly rises, with a peak value generally greater than 4. However, the CIF curve of a shear crack does not show a rapid rise, with a peak value is generally about 0.

5.2 Difference of Mixed Cracks

The previous research on mixed crack separation suffered from a lack of specificity and precision. The CIF calculation model further refined and quantified the mixed cracks. Complex crack coalescence forms can be defined based on the different degrees of control factors, dominant time, and dominant section of tensile or shear during the crack coalescence process. Both TS and ST cracks share the common factor that tension is the direct cause of crack
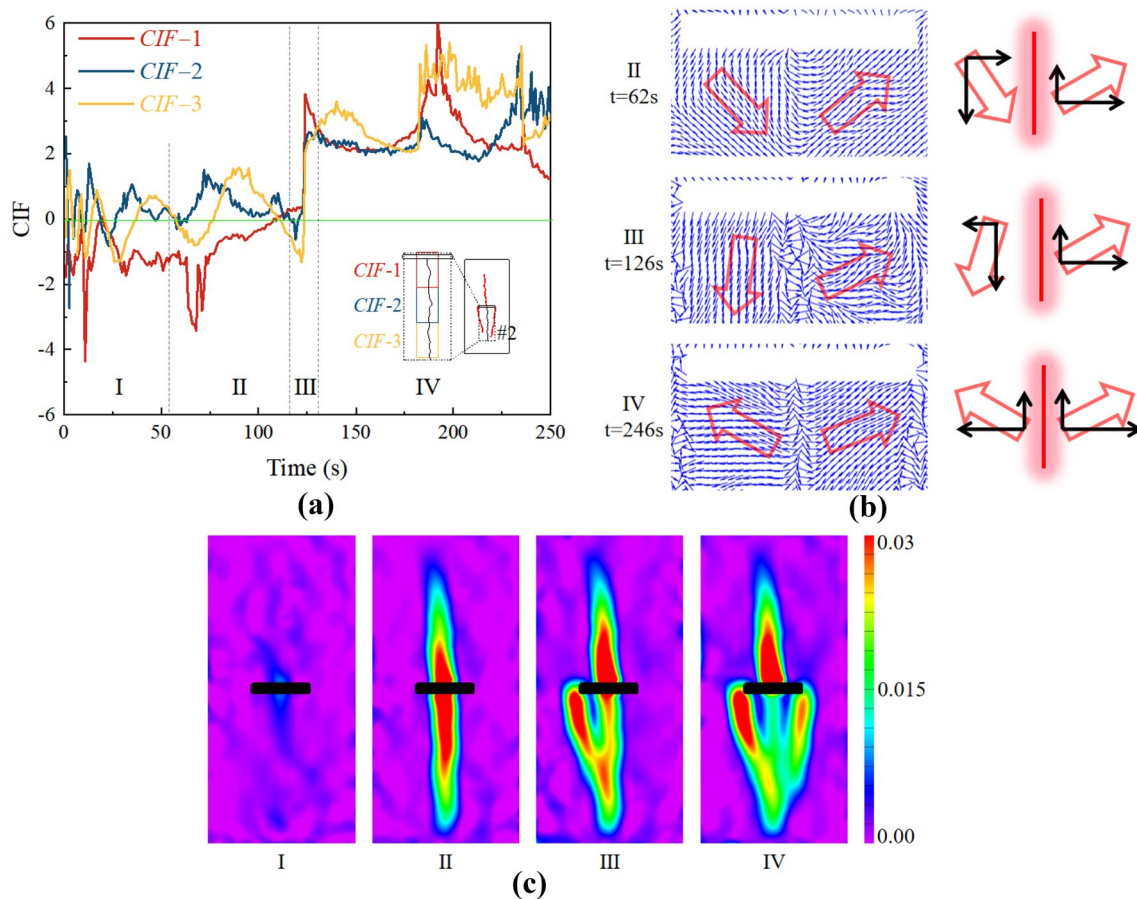
Fig. 26 Results of crack type determination models for crack #2 of S-0-1

coalescence, but other factors are completely different. TS cracks are less dominated by shear, with less extrusion and friction marks on the crack surface, while ST cracks are predominantly dominated by shear, with a broader range in terms of dominant time and section. The CIF values also distinguish between the two types of cracks, with TS cracks having a higher peak value of CIF, even greater than 6, while ST cracks have a CIF peak value around 2. This method has effectively quantified the disparities between these distinct crack types.

There are also obvious differences in the CIF curves between ST cracks. Specifically, the shear-dominated mixed cracks have two different spatial and temporal modes. The displacement vectors also prove the difference between the two types of cracks, representing two different ways of defining them. Figure 23 shows that the #3 crack in SC-0-1 has obvious shear strain characteristics in the initial and intermediate sections during the entire crack propagation process, while the terminal section shows obvious tensile strain characteristics. The crack displacement vector in Fig. 19 also shows the displacement characteristics at different sections of the crack. This type of crack is a

spatially defined shear-tensile mix and is named ST-space. Figure 24 shows the propagation process of the #3 crack in SC-45-2, where the crack is mainly influenced by shear during the propagation stages and later affected by tension to a certain extent. Figure 20 shows crack displacement vector at different times, confirming this point. This type of crack is a temporally defined shear-tensile mix and is named ST-time.

5.3 Summary of Crack Types

The conventional classification of crack types can vividly depict fracture behaviors of specimens, but it is important to note that traditional identification methods are based on visual inspection, which requires further quantitative proof. In some cases, applying a classification based on visual observation can lead to ambiguous results. The crack evaluation system proposed in this study eliminates the confusion inherent in crack type determination.

Based on distribution image of cracks, main strain field ε_1, shear strain field ε_{xy}, displacement trends lines around the cracks, and the CIF curve, all cracks are reassessed

Table 3 Summary of crack types for specimens containing different flaw widths

Specimen ID	Real image	Crack image	ε_1	ε_{xy}	Traditional crack determination	Tensile ratio Shear ratio Mixed ratio	Crack determination
S-0-1					#1, #2: Tensile crack #3, #4: Tensile crack or Mixed crack	60.7% 20.9% 18.4%	#1: T #2: T #3: TS #4: TS
S-45-2					#1, #2: Mixed tensile-shear crack	60.6% 19.6% 19.8%	#1: TS #2: TS
S-90-1					#1, #2, #3: Tensile crack	68.1% 14.4% 17.5%	#1: T #2: T #3: TS
SC-0-1					#1, #2: Tensile crack #3, #4: Tensile crack or Mixed crack	56.2% 17.3% 26.5%	#1: T #2: T #3: ST-space #4: ST-space
SC-45-2					#1, #2: Wing crack #3: Anti-wing crack #4: Secondary crack	58.5% 21.8% 19.7%	#1: TS #2: TS #3: ST-time #4: S
SC-90-1					#1: #3, #4: Secondary crack #2: Tensile crack	62.1% 15.6% 22.3%	#1: ST-time #2: T #3: TS #4: ST-time

and summarized in Table 3. The traditional method of crack classification is primarily based on previous scholars' research methods and conclusions (Niu et al. 2019; Sagong and Bobet 2002; Wong and Einstein 2009). For instance, #3 and #4 crack of S-0-1 exhibit a linear shape, propagating approximately perpendicular to the direction of maximum compression. From a traditional perspective, #3 and #4 crack are considered to be tensile cracks, but

the ε_{xy} indicates that they exhibit shear strain, which creates significant confusion. However, with the use of the DDTL model and CIF model proposed in this study, the classification of crack types is clear. Cracks #3 and #4 of S-0-1 have a CIF value of about −1 at the initiation stage and a CIF value of about 2 at the coalescence stage, with a curve form similar to that shown in Fig. 22. Therefore, cracks #3 and #4 are classified as TS type crack.

The percentages of tensile, shear and, mixed cracks for different specimens in Table 3 are obtained based on AF-RA method data (Du et al. 2020; Shi et al. 2023). The determination of crack types based on AE data verifies the reliability of the CIF model in determining crack types. For instance, comparing SC-0-1 to S-0-1, the former shows a mixed crack type leaning towards shear, resulting in a proportion of only 56.2% of tensile cracks, while the latter displays a mixed crack type leaning towards tension, resulting in a 60.7% proportion of tensile cracks. Comparing S-90-1 to S-0-1 and S-45-2, tensile cracks are predominant in the former, but not entirely. The AE data reveal that S-90-1 has a shear proportion of 14.4%, and the CIF model confirms that crack #3 has some shear features, indicating that it is a tensile-shear (TS) crack. It is noteworthy that the CIF model can provide quantitative results for a specific crack, which makes up for the shortcomings of the statistical analysis method based on the proportion of crack types obtained from AE data.

The CIF model offers a succinct and straightforward approach to determine crack types, aiming to develop more precise and reliable tools for characterizing and predicting the emergence of new failure modes in complex conditions. Although this study focuses on the fracture process of a sandstone specimen with a single flaw under uniaxial loading, the crack type classification methods can likely be extended to the broader study of rock fracture processes. Undoubtedly, the present model holds substantial potential for enhancement. Relying on two-dimensional apparent strain field data of the test specimen, the performance of the model depends on the accuracy of these data. Moreover, its current capability is restricted to discerning plane cracks, and further improvements are needed to accommodate the assessment of three-dimensional cracks. By applying these approaches, researchers can identify and classify different crack types, which can help them to better understand the mechanics of rock fracture and develop effective strategies for mitigating rock-related hazards.

6 Conclusions

The purpose of this study is to enhance comprehension of crack type determination and coalescence mechanism of cracks. The AE technique and DIC technique were used to determine the percentage of different types of cracks in the specimen and capture displacement information on the surface of specimen, respectively. Subsequently, the CIF model is established to quantitatively determine five distinct crack coalescence modes. The main conclusions of this study are as follows:

1. The width of the flaw significantly affected the type of crack. Specifically, the increase in flaw width affects the displacement form of the flaw tip, thereby affecting the coalescence mode of the crack. Meantime, an increase in flaw width correlates with a heightened prevalence of shear-type cracks within the specimen.
2. The introduction of the DDTL is proposed to refine crack classification. Six distinct displacement trend lines, directly contributing to crack extension are identified. The CIF curve obtained from the CIF calculation model showed that tensile and shear displacements jointly affected the early stage of crack coalescence, and the coalescence of cracks is the result of the alternating effects between shear and tension. The crack types are refined into T crack, S crack, TS crack, ST-space crack, and ST-time crack.
3. The CIF calculation model is established to quantify the dominant factors of crack coalescence. Significantly divergent CIF peak values are observed for different crack types during the coalescence stage. The final CIF peak value of tensile cracks is generally greater than 6, while that of shear cracks is generally about 0. The final CIF peak value of TS cracks is generally greater than 4, while that of ST cracks is around 2.
4. The CIF calculation model provides more efficient, cost-effective, and scalable solutions for disaster warning, crack coalescence analysis, and structural damage assessment in real rock engineering.

Data Availability The data underlying this article will be shared on reasonable request to the corresponding author.

Declarations

Conflict of interest The authors declared that they have no conflicts of interest.

References

Aliabadian Z, Zhao G, Russell AR (2019) Crack development in transversely isotropic sandstone discs subjected to Brazilian tests observed using digital image correlation. Int J Rock Mech Min 119:211–221

Aliabadian Z, Sharafisafa M, Tahmasebinia F, Shen L (2021) Experimental and numerical investigations on crack development in 3d printed rock-like specimens with pre-existing flaws. Eng Fract Mech 241:107396

Baqersad J, Poozesh P, Niezrecki C, Avitabile P (2017) Photogrammetry and optical methods in structural dynamics—a review. Mech Syst Signal Process 86:17–34

Bobet A, Einstein HH (1998) Fracture coalescence in rock-type materials under uniaxial and biaxial compression. Int J Rock Mech Min Sci Geomech Abstr 35(7):863–888

Cao P, Liu T, Pu C, Lin H (2015) Crack propagation and coalescence of brittle rock-like specimens with pre-existing cracks in compression. Eng Geol 187:113–121

Cao R, Yao R, Meng J, Lin Q, Lin H, Li S (2020) Failure mechanism of non-persistent jointed rock-like specimens under uniaxial loading: laboratory testing. Int J Rock Mech Min 132:104341

Cheng A, Zhou Y, Chen G, Huang S, Ye Z (2023) Acoustic emission characteristics and fracture mechanism of cemented tailings backfill under uniaxial compression: experimental and numerical study. Environ Sci Pollut R 30(19):55143–55157

Chu TC, Ranson WF, Sutton MA, Peters WH (1985) Applications of digital-image-correlation techniques to experimental mechanics. Exp Mech 25(3):232–244

Dong T, Cao P, Lin Q, Liu Z, Xiao F, Zhang Z (2022) Fracture evolution of artificial composite rocks containing interface flaws under uniaxial compression. Theor Appl Fract Mech 120:103401

Dong T, Cao P, Wang F, Zhang Z, Xiao F (2023) Strain field evolution and crack coalescence mechanism of composite strength rock-like specimens with sawtooth interface. Theor Appl Fract Mech 126:103947

Du K, Li X, Tao M, Wang S (2020) Experimental study on acoustic emission (Ae) characteristics and crack classification during rock fracture in several basic lab tests. Int J Rock Mech Min 133:104411

Fan W, Yang H, Jiang X, Cao P (2021) Experimental and numerical investigation on crack mechanism of folded flawed rock-like material under uniaxial compression. Eng Geol 291:106210

Gao M, Xie J, Gao Y et al (2021) Mechanical behavior of coal under different mining rates: a case study from laboratory experiments to field testing. Int J Min Sci Technol 31(5):825–841

Ha YD, Lee J, Hong J (2015) Fracturing patterns of rock-like materials in compression captured with peridynamics. Eng Fract Mech 144:176–193

Haeri H, Shahriar K, Marji MF, Moarefvand P (2014) Cracks coalescence mechanism and cracks propagation paths in rock-like specimens containing pre-existing random cracks under compression. J Cent South Univ 21(6):2404–2414

Han Z, Li D, Li X (2022) Effects of axial pre-force and loading rate on mode i fracture behavior of granite. Int J Rock Mech Min 157:105172

Ingraffea AR, Heuze FE (1980) Finite element models for rock fracture mechanics. Int J Numer Anal Methods Geomech 4(1):25–43

Irwin GR (1957) Analysis of stress and strains near the end of a crack extension force. J Appl Mech 24:361–364

Jiefan H, Ganglin C, Yonghong Z, Ren W (1990) An experimental study of the strain field development prior to failure of a marble plate under compression. Tectonophysics 175(1):269–284

Lin Q, Cao P, Wen G, Meng J, Cao R, Zhao Z (2021) Crack coalescence in rock-like specimens with two dissimilar layers and pre-existing double parallel joints under uniaxial compression. Int J Rock Mech Min 139:104621

Liu T, Lin B, Zheng C, Zou Q, Zhu C, Yan F (2015) Influence of coupled effect among flaw parameters on strength characteristic of precracked specimen: application of response surface methodology and fractal method. J Nat Gas Sci Eng 26:857–866

Liu X, Liu Z, Li X, Gong F, Du K (2020) Experimental study on the effect of strain rate on rock acoustic emission characteristics. Int J Rock Mech Min 133:104420

Liu L, Li H, Li X, Wu D, Zhang G (2021) Underlying mechanisms of crack initiation for granitic rocks containing a single pre-existing flaw: insights from digital image correlation (Dic) analysis. Rock Mech Rock Eng 54(2):857–873

Long XT, Wang GL, Lin WJ, Wang J, He ZQ, Ma JC, Yin XF (2023) Locating geothermal resources using seismic exploration in Xian county, China. Geothermics 112:102747

Miao S, Pan P, Hou W, Li M, Wu Z (2022) Determination of mode I fracture toughness of rocks with field fitting and J-integral methods. Theor Appl Fract Mech 118:103263

Munoz H, Taheri A, Chanda EK (2016) Pre-peak and post-peak rock strain characteristics during uniaxial compression by 3D digital image correlation. Rock Mech Rock Eng 49(7):2541–2554

Nikolic M, Ibrahimbegovic A (2015) Rock mechanics model capable of representing initial heterogeneities and full set of 3D failure mechanisms. Comput Method Appl Mech Eng 290:209–227

Niu Y, Zhou XP, Zhang JZ, Qian QH (2019) Experimental study on crack coalescence behavior of double unparallel fissure-contained sandstone specimens subjected to freeze-thaw cycles under uniaxial compression. Cold Reg Sci Technol 158:166–181

Niu Y, Zhou X, Berto F (2020) Evaluation of fracture mode classification in flawed red sandstone under uniaxial compression. Theor Appl Fract Mech 107:102528

Ohno K, Ohtsu M (2010) Crack classification in concrete based on acoustic emission. Constr Build Mater 24(12):2339–2346

Peters WH, Ranson WF (1982) Digital imaging techniques in experimental stress analysis. Opt Eng 21(3):213427

Qian R, Feng G, Guo J, Wang P, Wen X, Song C (2022) Experimental investigation of mechanical characteristics and cracking behaviors of coal specimens with various fissure angles and water-bearing states. Theor Appl Fract Mech 120:103406

Sagong M, Bobet A (2002) Coalescence of multiple flaws in a rock-model material in uniaxial compression. Int J Rock Mech Min Sci (oxford, England: 1997) 39(2):229–241

Shams G, Rivard P, Moradian O (2023a) Observation of fracture process zone and produced fracture surface roughness in granite under brazilian splitting tests. Theor Appl Fract Mech 125:103680

Shams G, Rivard P, Moradian O (2023b) Micro-scale fracturing mechanisms in rocks during tensile failure. Rock Mech Rock Eng 56(6):4019–4041

Sharafisafa M, Shen L, Xu Q (2018) Characterisation of mechanical behaviour of 3D printed rock-like material with digital image correlation. Int J Rock Mech Min 112:122–138

Sharafisafa M, Shen L, Zheng Y, Xiao J (2019) The effect of flaw filling material on the compressive behaviour of 3D printed rock-like discs. Int J Rock Mech Min 117:105–117

Shi Z, Li J, Wang J (2022) Research on the fracture mode and damage evolution model of sandstone containing pre-existing crack under different stress paths. Eng Fract Mech 264:108299

Shi Z, Li J, Wang J (2023) Energy evolution and fracture behavior of sandstone under the coupling action of freeze-thaw cycles and fatigue load. Rock Mech Rock Eng 56(2):1321–1341

Si XF, Luo Y, Luo S (2024) Influence of lithology and bedding orientation on failure behavior of "D" shaped tunnel. Theor Appl Fract Mech 129:104219

Wang Y, Zhang B, Gao SH, Li CH (2021) Investigation on the effect of freeze-thaw on fracture mode classification in marble subjected to multi-level cyclic loads. Theor Appl Fract Mech 111:102847

Wang J, Li J, Shi Z, Chen J (2022a) Fatigue damage and fracture evolution characteristics of sandstone under multistage intermittent cyclic loading. Theor Appl Fract Mech 119:103375

Wang J, Li J, Shi Z, Chen J, Lin H (2022b) fatigue characteristics and fracture behaviour of sandstone under discontinuous multilevel constant-amplitude fatigue disturbance. Eng Fract Mech 274:108773

Wang F, Xie HP, Zhou CT, Wang ZH, Li CB (2023a) Combined effects of fault geometry and roadway cross-section shape on the collapse

behaviors of twin roadways: an experimental investigation. Tunn Undergr Space Technol 137:105106

Wang F, Zhang P, Li KH, Wang C, Cui PF (2023b) Mechanical and fracture characteristics of single tunnel under the induced effect of a key joint. Arch Civ Mech Eng 23:206

Wong LNY, Einstein HH (2009) Systematic evaluation of cracking behavior in specimens containing single flaws under uniaxial compression. Int J Rock Mech Min Sci 46(2):239–249

Wu H, Fan G (2020) An overview of tailoring strain delocalization for strength-ductility synergy. Prog Mater Sci 113:100675

Wu Z, Wong LNY (2012) Frictional crack initiation and propagation analysis using the numerical manifold method. Comput Geotech 39:38–53

Xie S, Lin H, Duan H, Chen Y (2023) Modeling description of interface shear deformation: a theoretical study on damage statistical distributions. Constr Build Mater 394:132052

Zafar S, Hedayat A, Moradian O (2022a) Micromechanics of fracture propagation during multistage stress relaxation and creep in brittle rocks. Rock Mech Rock Eng 55(12):7611–7627

Zafar S, Hedayat A, Moradian O (2022b) Evolution of tensile and shear cracking in crystalline rocks under compression. Theor Appl Fract Mech 118:103254

Zhang Z, Deng J (2020) A new method for determining the crack classification criterion in acoustic emission parameter analysis. Int J Rock Mech Min 130:104323

Zhang X, Wong LNY (2011) Cracking processes in rock-like material containing a single flaw under uniaxial compression: a numerical study based on parallel bonded-particle model approach. Rock Mech Rock Eng 45:711–737

Zhang X, Wong LNY (2014) Displacement field analysis for cracking processes in bonded-particle model. Bull Eng Geol Environ 73(1):13–21

Zhang R, Zhao C, Yang C, Xing J, Morita C (2021) A comprehensive study of single-flawed granite hydraulically fracturing with laboratory experiments and flat-jointed bonded particle modeling. Comput Geotech 140:104440

Zhang K, Jiang Z, Liu X, Zhang K, Zhu H (2022) Quantitative characterization of the fracture behavior of sandstone with inclusions: experimental and numerical investigation. Theor Appl Fract Mech 121:103429

Zhao X, Zhang H, Zhu W (2014) Fracture evolution around pre-existing cylindrical cavities in brittle rocks under uniaxial compression. Trans Nonferr Metal Soc 24(3):806–815

Zhou Z, Cao P, Ye Z (2014a) Crack propagation mechanism of compression-shear rock under static-dynamic loading and seepage water pressure. J Cent South Univ 21(4):1565–1570

Zhou XP, Cheng H, Feng YF (2014b) An experimental study of crack coalescence behaviour in rock-like materials containing multiple flaws under uniaxial compression. Rock Mech Rock Eng 47(6):1961–1986

Zhou XP, Bi J, Qian QH (2015) Numerical simulation of crack growth and coalescence in rock-like materials containing multiple pre-existing flaws. Rock Mech Rock Eng 48(3):1097–1114

Zhou CT, Xu CH, Karakus M, Shen JY (2019) A particle mechanics approach for the dynamic strength model of the jointed rock mass considering the joint orientation. Int J Numer Anal Methods Geomech 43(18):2797–2815

Zhou ZL, Cai X, Li XB, Cao WZ, Du XM (2020) Dynamic response and energy evolution of sandstone under coupled static-dynamic compression; insights from experimental study into deep rock engineering applications. Rock Mech Rock Eng 53(3):1305–1331

Zhou XP, Fu YH, Wang Y, Zhou JN (2022a) Experimental study on the fracture and fatigue behaviors of flawed sandstone under coupled freeze-thaw and cyclic loads. Theor Appl Fract Mech 119:103299

Zhou T, Chen J, Xie H, Zhou C, Wang F, Zhu J (2022b) Failure and mechanical behaviors of sandstone containing a pre-existing flaw under compressive-shear loads: insight from a digital image correlation (Dic) analysis. Rock Mech Rock Eng 55(7):4237–4256